

1 Seasonal changes in sea ice kinematics and deformation 2 in the Pacific Sector of the Arctic Ocean in 2018/19

3 Ruibo Lei¹, Mario Hoppmann², Bin Cheng³, Guangyu Zuo^{1,4}, Dawei Gui^{1,5},
4 Qiongqiong Cai⁶, H. Jakob Belter², Wangxiao Yang⁴

5 ¹ Key Laboratory for Polar Science of the MNR, Polar Research Institute of China, Shanghai, China.

6 ² Alfred-Wegener-Institut Helmholtz-Zentrum für Polar- und Meeresforschung, Bremerhaven,
7 Germany.

8 ³ Finnish Meteorological Institute, Helsinki, Finland.

9 ⁴ College of Electrical and Power Engineering, Taiyuan University of Technology, Taiyuan, China.

10 ⁵ Chinese Antarctic Center of Surveying and Mapping, Wuhan University, Wuhan, China.

11 ⁶ National Marine Environmental Forecasting Center of the MNR, Beijing, China.

12 *Correspondence to:* Ruibo Lei (leiruibo@pric.org.cn)

13
14 **Abstract.** Arctic sea ice kinematics and deformation play significant roles in heat and momentum
15 exchange between ~~the~~ atmosphere and ocean, and ~~at the same time they~~ have ~~a~~ profound impacts on
16 biological processes and biogeochemical cycles. However, ~~the~~ mechanisms regulating their changes on
17 ~~at~~ seasonal scales ~~and their spatial variability~~ remain poorly understood. Using position data ~~recorded by~~
18 ~~of~~ 32 buoys in the Pacific sector of the Arctic Ocean (PAO), we characterized ~~the~~ spatiotemporal
19 variations in ice kinematics and deformation for autumn–winter 2018/19, ~~during over~~ the transition from
20 ~~a~~ melting ~~sea ice regime ice~~ to a near consolidated ice pack. In autumn, the response of ~~the~~ sea ice drift to
21 wind ~~and inertial~~ forcing ~~and its inertial oscillation~~ were stronger in the southern and western ~~PAO~~
22 ~~compared to than in~~ the northern and eastern ~~parts of the~~ PAO. These spatial heterogeneities ~~decreased~~
23 gradually ~~weakened~~ from autumn to winter, in line with the increases in ice concentration and thickness.
24 Correspondingly, ice deformation ~~became becomes~~ much more localized as the sea ice mechanical
25 strength ~~increased~~ ~~increases~~, with the area proportion occupied by the strongest ~~(15%)~~ ice deformation
26 decreasing by about 50 % from autumn to winter. During the freezing season, ice deformation rate in the
27 northern ~~part of the~~ PAO was about 2.5 times ~~higher than that~~ in the western ~~PAO and part~~ probably
28 related to the higher spatial heterogeneity of oceanic and atmospheric forcing in the north. North–south
29 and east–west gradients in sea ice kinematics and deformation ~~within of~~ the PAO, as observed in this

30 study, are likely to become more pronounced in the future as a result of a longer melt season, especially
31 in the western and southern parts.

32 1 Introduction

33 The Pacific sector of Arctic Ocean (PAO) includes the Beaufort, Chukchi, and East Siberian Seas, as
34 well as the Canadian and Makarov Basins. Among all the different sectors of the Arctic Ocean, the PAO
35 exhibited the largest decreases in both seasonal summer sea ice (Comiso et al., 2017) and multi-year sea
36 ice (MYI) (Serreze and Meier, 2018) are the largest in the PAO in recent decades. These changes are,
37 and are most likely attributed linked to an enhanced ice–albedo feedback (Steele and Dickinson, 2016),
38 increased Pacific water inflow (Woodgate et al., 2012), and a more pronounced enhanced Arctic Dipole
39 (Lei et al., 2016). In the PAO, MYI is mainly distributed north of the Canadian Arctic Archipelago
40 (Lindell and Long, 2016), suggesting a strong east–west gradient in sea ice thickness and strength. In
41 summer, the marginal ice zone (MIZ), defined as the area in which the where sea ice concentration is less
42 than 80 %, can reach as far north as 80° N (Strong and Rigor, 2013), thus the south–north gradient in sea
43 ice properties ice conditions in the PAO is expected to be larger compared to greater than that in other
44 sectors of the Arctic Ocean.

45 Sea ice deformation typically results from the divergence, convergence, and shear of ice floes and the
46 presence of shear stresses, which can enhance redistribution of ice thickness and/or sea ice production
47 by through creating the formation of leads and ridges (Hutchings and Hibler, 2008; Itkin et al., 2018).
48 Loss of MYI and a decreased ice thickness weakens the Arctic sea ice cover, increases floe mobility
49 (Spreen et al., 2011), and promotes ice deformation (Kwok, 2006). Leads forming between ice floes
50 increase heat transfer from the ocean to the atmosphere, a process that is particularly important in winter
51 because of the large temperature gradient (Alam and Curry, 1998). In summer, cracks, leads or polynyas
52 within the pack ice represent serve as windows that expose the ocean to more sunlight. They may, which
53 significantly alters many biological processes and biogeochemical cycles, for example supporting large
54 such as promoting under-ice haptophyte algae blooms (Assmy et al., 2017). Under converging
55 conditions, ice blocks are packed randomly during the formation of sea ice pressure ridges, creating
56 water-filled voids that act as thermal buffers for subsequent ice growth (Salganik et al., 2020). The high
57 porosity of pressure ridges creates provides an abundance of nutrients for ice algae communities. As a

58 result, pressure ridges can become biological hotspots (Fernández-Méndez et al., 2018). Thus, [accurate](#)
59 characterizations of sea ice deformation are not only relevant ~~to~~ ~~for~~ a better understanding of ice
60 dynamics and ~~their~~ ~~its~~ roles in Arctic climate ~~system~~ ~~current change~~, but especially also of [the evolution](#)
61 [of](#) ice-associated ecosystems.

62 In the PAO, the generally anticyclonic Beaufort Gyre (BG) ~~governs a~~ ~~generates~~ sea ice motion that is
63 clockwise on average. The boundary and strength of the BG are mainly regulated by the Beaufort High
64 (BH) (Proshutinsky et al., 2009; Lei et al., 2019). An anomalously low BH can result in a reversal of
65 wind and ice motion in the PAO that is normally anticyclonic (Moore et al., 2018). Under a positive
66 Arctic Dipole Anomaly (DA), more sea ice from the PAO is transported to the Atlantic sector of the
67 Arctic Ocean (AAO), i.e., promoting ice advection from the BG system to the Transpolar Drift Stream
68 (TDS) (Wang et al., 2009). In summer, such a regime would stimulate the ice–albedo feedback and
69 accelerate sea ice retreat [in the PAO](#) (Lei et al., 2016). The loss of [PAO](#) summer sea ice ~~in the PAO~~
70 [observed](#) during the ~~recent~~ ~~last~~ four decades can be explained [by an increase of](#) ~~using the increased~~ ice
71 advection from the PAO to the AAO by 9.6% (Bi et al., 2019). In the zonal direction, the enhanced
72 anticyclonic circulation in the PAO, [which is majorly related to a positive BH anomaly \(Lei et al.,](#)
73 [2019\)](#), can result in [a larger](#) ~~more~~ ice advection from the Beaufort and Chukchi ~~seas~~ ~~Seas~~ to the East
74 Siberian Sea (Ding et al., 2017). The response of sea ice advection in this region to interannual
75 variations of atmospheric circulation patterns has been studied extensively (e.g., Vihma et al., 2012), but
76 investigations [of ice deformation](#) on a seasonal scale are relatively scarce.

77 From a dynamical perspective, sea ice consolidation has been related to the strength of the inertial signal
78 of sea ice motion (Gimbert et al., 2012), Ice–Wind Speed Ratio (IWSR) (Haller et al., 2014), localization,
79 intermittence and space–time coupling of sea ice deformation (Marsan et al., 2004), as well as ~~to~~ the
80 response of ice deformation to wind forcing (Haller et al., 2014). The inertial oscillation is caused by the
81 earth’s rotation and is stimulated by sudden changes in external forces, ~~mainly~~ ~~majorly~~ due to enhanced
82 wind stress on the ~~ice-ocean interface and surface mixed layer~~ ~~ice-ocean mixing layer~~ caused by
83 storms/cyclones or moving fronts of extreme weather events (e.g., Lammert et al., 2009; Gimbert et al.,
84 2012). It [usually](#) is weakened [by the friction at the ice-ocean interface](#) ~~due to surface friction~~ and
85 internal ice stresses. The localization and intermittence of sea ice deformation indicate the degree of
86 constraint for its spatial range and temporal duration (Rampal et al., 2008). Space-time coupling
87 demonstrates the temporal or spatial dependence ~~for~~ ~~of~~ the spatial or temporal scaling laws of ice

88 deformation, which can indicate the brittle behaviour of sea ice deformation (Rampal et al., 2008;
89 Marsan and Weiss, 2010). The inertial oscillations of ~~Arctic~~ sea ice motion (Gimbert et al., 2012) and
90 the IWSR (Spren et al., 2011) in the Arctic Ocean have been increasingly associated with reduced sea
91 ice thickness and concentration.

92 The application of drifting ice buoys to determine the properties and seasonal cycle of the atmosphere,
93 ocean, and sea ice on a basin scale and year-round has been an emerging technique ~~field~~ in polar
94 research in recent years. For example, drifting buoys are a suitable ~~good~~ tool to track relative ice
95 motion. However, ~~because of the~~ usually limited presence number of such buoys ~~deployed~~ in ~~any a~~ given
96 region and season due to ~~financial and logistical constraints has made it~~ cost and logistical limitation, it
97 ~~has so far been~~ difficult so far to accurately distinguish spatial variability and temporal changes in sea ice
98 kinematics and deformation ~~from existing buoy data~~ in the PAO. During spring 2003, the deformation of
99 a single lead in the Beaufort Sea was investigated using Global Positioning System (GPS) receivers
100 (Hutchings and Hibler, 2008). ~~The~~ Sea ice deformation and its length scaling law in the southern ~~south~~
101 ~~of the~~ PAO during March–May have been estimated before by Hutchings et al. (2011 and 2018) and
102 Itkin et al. (2017). Based on the dispersion characteristics of ice motion estimated from buoy data
103 recorded in the southern ~~using the data obtained from buoys deployed on the ice in the south of the~~
104 Beaufort Sea, Lukovich et al. (2011) found that the scaling law of absolute zonal dispersion is about
105 twice that at in the meridional direction. Lei et al. (2020a and 2020b) used data recorded by two buoy
106 arrays deployed in the northern ~~north of~~ PAO to describe the influence of cyclonic activities and the
107 summer sea ice regime on the seasonal evolution ~~in of~~ sea ice deformation. In addition to in-situ buoy
108 data, ~~h~~High resolution satellite images (e.g., Kwok, 2006) and sea ice numerical models (e.g., Hutter et
109 al., 2018) have been ~~used~~ to identify spatial and temporal variations of ice deformation on at the basin
110 scale. RADARSAT data for example ~~collected from the western Arctic Ocean~~ revealed that the length
111 scaling law of ice deformation in the western Arctic Ocean ~~would~~ increased in summer as the ice pack
112 weakens and internal stresses ~~are not as readily~~ cannot be transmitted over long distances compared to
113 ~~as in~~ winter (Stern and Lindsay, 2009). However, an assessment of the ability of satellite techniques ~~their~~
114 ability to accurately characterize ice deformation, which usually ~~often~~ occurs on much smaller scales
115 than the image resolution and over much shorter periods than their retrieval intervals ~~small scales and over~~
116 ~~short periods~~ (Hutchings and Hibler, 2008), still requires more ground-truthing data as provided
117 measured by drifting buoys. So far, a comprehensive picture of spatial and seasonal variations of sea

118 ice kinematics and deformation for the PAO region has not yet been obtained, and our understanding is
119 particularly limited with respect to the transition from the melting season to a near rigid-lid
120 [consolidated](#) ice pack in winter.

121 In order to address ~~the this~~ knowledge gaps [outlined above](#), 27 drifting buoys were deployed on sea ice in
122 the PAO during August and September 2018 by the Chinese National Arctic Research Expedition
123 (CHINARE) and the T-ICE expedition led by the Alfred-Wegener-Institute. In this study, we combined
124 the data measured by these buoys with other available buoy data from the International Arctic Buoy
125 Programme (IABP) to identify the spatial variability of sea ice kinematics [and deformation parameters](#)
126 in the PAO from melting to freezing season, and linked these results to the atmospheric forcing
127 responsible for the observed changes in ice dynamics.

128 **2 Data and Methods**

129 **2.1 Deployment of drifting buoys**

130 Four types of buoys were used in this study (Fig. 1). ~~They are:~~ the Snow and Ice Mass Balance Array
131 (SIMBA) buoy manufactured by the Scottish Association for Marine Science Research Services Ltd,
132 Oban, Scotland; the Snow Buoy (SB) designed by the Alfred-Wegener-Institute and manufactured by
133 MetOcean Telematics, Halifax, Canada; the ice Surface Velocity Program drifting buoy (iSVP) also
134 manufactured by MetOcean Telematics; and the ice drifter manufactured by the Taiyuan University of
135 Technology (TUT), China. All buoys ~~were are~~ equipped with GPS receivers providing a positioning
136 accuracy of better than 5 m, and regularly reported their data to a land-based receiving [station-system](#)
137 using the Iridium satellite network.

138 During the CHINARE, 9 SIMBA buoys and 11 TUT buoys were deployed in a narrow zonal section [of](#)
139 ~~between~~ 156° ~~W and~~ 171° W and a wide meridional range [between of](#) 79.2° ~~N and~~ 84.9° N in August
140 2018 (Figs. 1 and 2). This deployment scheme was designed to facilitate the analysis of changes in ice
141 kinematics from the loose MIZ to the consolidated Pack Ice Zone (PIZ). Of these 20 buoys, 15 were
142 deployed in the northern part of the PAO as a cluster within close distance of each other (black circles in
143 Fig. 2) to allow [an](#) estimations of ice deformation rates. In addition, data from five SIMBAs and two SBs
144 deployed by the T-ICE expedition in the Makarov Basin during September 2018 (Figs. 1 and 2) were also
145 used to estimate ice deformation rates. Because the ice thickness at the deployment sites was comparably

146 large (1.22 to 2.49 m), the buoys were able to survive ~~into until~~-winter and beyond. Position data from
147 one iSVP deployed during the previous CHINARE in 2016 (Lei et al., 2020a) and four other IABP
148 buoys were also included in this study. The IABP buoys were deployed by the British Antarctic Survey
149 and Environment Canada in the east of the PAO during ~~late~~-August ~~or late~~-September 2018. Here we
150 use the position data from these 32 buoys to describe spatial variations in ice kinematics (Fig. 2) between
151 August 2018 and February 2019. We chose this study period because it represents a transition period
152 during which the mechanical properties of sea ice are expected to change considerably (e.g., Herman and
153 Glowacki, 2012; Hutter et al., 2018). ~~Also, s~~Some buoys ceased operation by March 2019, ~~while~~
154 ~~two-thirds of them. Two thirds of the buoys~~ (22) continued to send data until or beyond the end of the
155 study period. ~~During this study period, T~~he buoy trajectories ~~of the buoys~~ during the study period
156 ~~roughly~~ covered the region of 76° ~~–~~87° N and 155° E ~~–~~110°W, which we define here as our study
157 region.

158 2.2 Analysis of sea ice kinematic characteristics

159 All buoys ~~were configured to had~~a sampling interval of either 0.5 or 1 h. Prior to the calculation of
160 ice drift velocity, position data measured by the buoys were interpolated to a regular interval (τ) of 1 h.
161 To quantify meridional (zonal) variabilities of ice kinematic properties, we used data from buoys that
162 were within one standard deviation of the average longitude (latitude). ~~This constraint helped, which~~
163 ~~helps~~ to minimize ~~the~~ influence of ~~the~~ zonal (meridional) difference on ~~the~~ meridional (zonal)
164 variabilities. ~~The resulting This constraint leads to a~~ meridional extent ~~for the assessment of the zonal~~
165 ~~variabilities of ice kinematics ranged ranging~~ from 350 to 402 km, ~~while the when the zonal~~
166 ~~variabilities of ice kinematics were assessed and a~~ zonal extent ~~ranging from 195 to 285 km~~ for the
167 assessment of ~~the~~ meridional variabilities ~~ranged from 195 to 285 km~~. Their seasonal changes can be
168 considered as moderate (<40%) although ~~the a~~ divergence of the ~~buoys floes~~ occurred at all times. If
169 ~~we use a~~ half the standard deviations ~~is used~~ to constrain the calculation range, there ~~would is be~~ no
170 essential change in the identified meridional/zonal dependencies of ice kinematics from those obtained
171 using one standard deviation. Thus, we consider our evaluation method as robust. Meridional
172 variabilities are related to the transition from the MIZ to the PIZ, while zonal variabilities indicate the
173 change between the region north of the Canadian Arctic Archipelago, where MYI coverage is usually
174 large (Lindell and Long, 2016) and the Makarov Basin, which is mainly covered by seasonal ice

175 (Serreze and Meier, 2018).

176 Two parameters were used to characterize sea ice kinematics. First, the IWSR was used to investigate
177 the response of the sea ice motion to wind forcing. Impacts of data resampling intervals ~~data at~~
178 ~~intervals between (1– and 48 h)~~, meridional and zonal spatial variabilities, intensity of wind forcing,
179 near-surface air temperature, and ice concentration on the IWSR were assessed. These parameters are
180 either related to spatiotemporal changes in atmospheric and sea ice conditions, or to the frequency
181 characteristics of ice and wind speeds. The data used to characterize the atmospheric forcing,
182 including sSea level air pressure (SLP), near-surface air temperature at 2 m (T_{2m}) and wind velocity
183 at 10 m (W_{10m}), were obtained from the ECMWF ERA-Interim reanalysis dataset (Dee et al., 2011).
184 Sea ice concentration was obtained from the Advanced Microwave Scanning Radiometer 2 (AMSR2)
185 (Spreen et al., 2008). To identify the state of the atmospheric forcing and the sea ice conditions
186 relative to the climatology, we also calculated anomalies of SLP, T_{2m} , W_{10m} , ice concentration, and ice
187 drift speed relative to the 1979–2018 averages. To estimate ice concentration anomalies, we used ice
188 concentration data from the Nimbus-7 Scanning Multichannel Microwave Radiometer (SMMR) and
189 its successors (SSM/I and SSMIS) (Fetterer et al., 2017) because they cover a longer period compared
190 to the than AMSR2 data. We used the daily product of sea ice motion (Tschudi et al., 2019 and 2020)
191 provided by the National Snow and Ice Data Center (NSIDC) to estimate anomalies of ice ~~drift~~ speed
192 anomalies. ~~However, this could can be only estimated for August–December 2018.~~ Because of the
193 ~~delayed release of NSIDC data, ice speed anomalies were only estimated for August–December 2018.~~

194 Second, the inertial motion index (IMI) was used to quantify the inertial component of the ice motion.
195 To obtain the IMI, we applied a Fast Fourier Transformation to normalized hourly ice velocities.
196 Normalized ice velocities were calculated by scaling the velocity values to monthly averages,
197 allowing seasonal change to be assessed independently of the magnitudes of ice velocities. The
198 frequency of the inertial oscillation varies with latitude according to as follows:

$$199 \quad f_0 = 2\Omega \sin \theta \quad (1)$$

200 where f_0 is the inertial frequency, Ω is the Earth rotation rate, and θ is the latitude. f_0 ranges from 2.01
201 to 1.94 cycles day⁻¹ between 90° N and 75° N. Rotary spectra calculated from sea ice velocity using
202 complex Fourier analysis were used to identify signals of inertial and or tidal origin, both of which

203 have a frequency of ~ 2 cycles day⁻¹ in the Arctic Ocean (Gimbert et al., 2012). According to Gimbert
204 et al. (2012), the complex Fourier transformation $\widehat{U}(\omega)$ is defined as:

$$205 \quad \widehat{U}(\omega) = \frac{1}{N} \sum_{t=t_0}^{t_{end}-\Delta t} e^{-i\omega t} (u_x + iu_y), \quad (2)$$

206 where N and Δt are the number and temporal interval of velocity samples, t_0 and t_{end} are the start and end
207 times of the temporal window, u_x and u_y are the zonal and meridional ice speeds at $t+0.5\Delta t$ on an
208 orthogonal geographical grid, and ω is the angular frequency. The IMI ~~was is~~ defined as the amplitude at
209 the negative-phase inertial frequency, i.e., $-f_0$, after the complex Fourier transformation. ~~We note that~~
210 ~~the energies that~~ contributed to the amplitude at $-f_0$ comprise the potential contributions from
211 quasi-semidiurnal inertial and tidal oscillations, ~~as well as and~~ the high-frequency components of wind
212 and oceanic forcing; while ~~that those~~ in the positive phase, f_0 , excludes contributions from the inertial
213 oscillation; and only comprises other components compared to that ~~at $-f_0$ in a negative phase~~. This is
214 because the spectral peaks associated with the tidal oscillation are roughly symmetric at positive and
215 negative phases as a first order approximation (Gimbert et al., 2012). On the contrary, the spectral peak
216 associated with the inertial oscillation is asymmetric and only occurs in the negative phase in the Arctic
217 Ocean. Thus, we can identify the seasonal changes in the contributions of the inertial oscillation by
218 comparing the amplitude at the negative-phase quasi-semidiurnal frequency, i.e., IMI, ~~with to~~ that in the
219 positive phase (hereinafter referred to as the positive-phase amplitude, short: PHA). Such method to
220 separate the inertial oscillation from the tidal oscillation has been used by Lammert et al. (2009), who
221 attempted to identify cyclone-induced inertial ice oscillation in Fram Strait. The background noise
222 originating from high-frequency components of wind and oceanic forcing can slightly shift the local
223 ~~maxima maximums slightly~~ from the targeted frequencies of the IMI and PHA (Geiger and Perovich,
224 2008). Thus, we identify the local maximum amplitude in the range of $-f_0 \pm 0.03$ for the IMI and in the
225 range of 2 ± 0.03 for the PHA. ~~such ranges can ensure~~ These ranges ensure that most
226 ~~quasi-semidiurnal signals can be identified~~ almost all quasi-semidiurnal signals won't be missed. If no
227 local maximum can be identified within the predefined ranges, we use the amplitudes at $-f_0$ and 2 as
228 the IMI and PHA, respectively. Such a situation is encountered in 15% of the IMI cases, and in 95% of
229 the PHA cases ~~rare for the IMI, i.e., approximately with 15% cases; while it is prevalent for the PHA,~~
230 ~~i.e., approximately with 95% cases~~. This implies ~~that an the~~ inertial oscillation is much more prevalent,

231 while the tidal oscillation can be ignored regardless of seasons and buoys under consideration. This
 232 result, which might be related to the fact that, throughout the study period, all the buoys drifted over the
 233 deep basins far waters beyond the continental shelf through the study period.

234 2.3 Analysis of sea ice deformation characteristics

235 Buoy position data were also ~~Ice positions were~~ used to estimate differential kinematic properties
 236 (DKPs) of the sea ice deformation field. The DKPs include divergence (*div*), shear (*shr*), and total
 237 deformation (*D*) rates of sea ice estimated within the area enclosed by any three buoys, as shown by
 238 Itkin et al. (2017). Following Hutchings and Hibler (2008), DKPs were calculated as follows:

$$239 \quad div = \frac{\partial u}{\partial x} + \frac{\partial v}{\partial y}, \quad (3)$$

$$240 \quad shr = \sqrt{\left(\frac{\partial u}{\partial x} - \frac{\partial v}{\partial y}\right)^2 + \left(\frac{\partial u}{\partial y} + \frac{\partial v}{\partial x}\right)^2}, \quad (4)$$

$$241 \quad \text{and } D = \sqrt{div^2 + shr^2}, \quad (5)$$

242 where $\frac{\partial u}{\partial x}$, $\frac{\partial u}{\partial y}$, $\frac{\partial v}{\partial x}$, and $\frac{\partial v}{\partial y}$ are the strain components on an orthogonal geographical grid. Sea ice strain
 243 rate was only estimated ~~only~~ for those buoy triangles with internal angles in excess of 15° and for ice
 244 speeds >larger than 0.02 m s⁻¹ to ensure a high accuracy (Hutchings et al., 2012). Total deformation *D*
 245 was used to characterize the spatial and temporal scaling laws as follows:

$$246 \quad D \propto L^{-\beta}, \quad (6)$$

$$247 \quad \text{and } D \propto \tau^{-\alpha}, \quad (7)$$

248 where *L* is the length scale, τ is the sampling interval, and β and α are spatial and temporal scaling
 249 exponents which indicate the decay rates of ~~the sea~~ ice deformation in the spatial or temporal domains.

250 These scaling laws can only indicate the fractal properties of the first moment of ice deformation
 251 because of the multi-fractal properties of ice deformation (e.g., Marsan et al., 2004; Hutchings et al.,
 252 2011 and 2018). To estimate the spatial exponent β for the CHINARE buoy cluster, the length scale
 253 was divided into three bins of 5–10, 10–20, and 20–40 km ~~for the CHINARE buoy cluster~~ because
 254 only few samples were outside these bins. To ~~the~~ estimate the temporal exponent α , the position data
 255 were resampled at to intervals of 1, 2, 4, 8, 12, 24, and 48 h. Because the T-ICE buoy cluster was
 256 mostly (> 70 %) assigned in to the ~~bin of~~ 40–80 km bin, data from this cluster were not suitable for
 257 the estimation of the scale effect. A space–time coupling index, *c*, denoting temporal (spatial)
 258 dependence of the spatial (temporal) scaling exponent, can be expressed as:

259 $\beta(\tau) = \beta_0 - c \ln(\tau)$, (8)

260 where β_0 is a constant. The areal localization index, $\delta_{15\%}$, was used to quantify the localization of the
261 strongest sea ice deformation, ~~which is~~ defined as the fractional area accommodating the largest 15 %
262 of the ice deformation in the research domain (Stern and Lindsay, 2009). The $\delta_{15\%}$ was calculated for
263 the ~~length bin of~~ 10–20 km ~~length bin~~ for the CHINARE buoy cluster, ~~since because~~ this bin contained
264 more samples to ensure a statistical rationality. To identify the influence of the temporal scale on the
265 localization of ice deformation, all data were resampled to intervals of 1, 2, 4, 8, 12, 24, and 48 h.

266 2.4 Atmospheric circulation pattern

267 ~~To identify the influence of atmospheric circulation patterns on sea ice kinematics and deformation,~~
268 ~~w~~We calculated the seasonal Central Arctic Index (CAI) and DA index to relate these large-scale
269 atmospheric circulation patterns to the potential of sea ice advection from the study region to the AAO
270 (Vihma et al., 2012; Bi et al., 2019), ~~).~~ ~~Further, we calculated~~ ~~and~~ the seasonal AO and BH indices to
271 relate them to the strength of the BG (Lei et al., 2019). Monthly SLP data north of 70° N obtained from
272 the NCEP/NCAR reanalysis I dataset were used to calculate the empirical orthogonal functions (EOF),
273 with the AO and DA as the first and second modes of the EOF (Wang et al., 2009). The CAI was defined
274 as the difference in SLP between 90° W and 90° E at 84° N (Vihma et al., 2012). The BH index was
275 calculated as the SLP anomaly over the domain of 75°–85° N, 170° E–150° W (Moore et al., 2018)
276 relative to 1979–2018 climatology.

277 3 Results and discussions

278 3.1 Spatial and seasonal changes in atmospheric and sea ice conditions

279 The BH index for autumn (September, October, and November) 2018 was moderate, ranking the tenth
280 highest in 1979–2018 (Fig. 3a). However, the BH index for the following winter (December, January,
281 and February) was much lower at –5.6 hPa, ranking the fourth lowest in 1979–2018 (Fig. 3b). Both,
282 CAI and DA, were positive in autumn 2018, but still within one standard deviation of the 1979–2018
283 climatology (Fig. 3c and 3e). However, both indices were strongly positive in winter 2018/19, ranking
284 the third and second highest in 1979–2018, respectively (Fig. 3d and 3f). The sea ~~Sea~~ ice in the PAO is
285 expected to be considerably impacted ~~considerably~~ by these seasonal changes in atmospheric
286 circulation patterns as a result of the enhanced northward advection of sea ice to the AAO (e.g., Bi et

287 al., 2019). As an example, ~~a pronounced extreme~~ sea ice reduction has been observed in the Bering Sea
288 in ~~late winter~~ March 2019, where sea ice extent was 70 %–80 % lower than normal (Perovich et al.,
289 2019).

290 Associated with the seasonal change in the BH index, there was a distinct contrast in the pattern of the
291 BG ~~from anticyclonic in autumn to cyclonic between autumn and in~~ winter. Wind vectors and ice drift
292 trajectories during autumn 2018 were generally clockwise, while those during the following winter
293 were counterclockwise. ~~The latter resulted in, with~~ all buoys drifting northeastward ~~and integrating~~
294 ~~into the TDS~~ from December 2018 onward ~~and integrating into the TDS, i.e., from anticyclonic to~~
295 ~~cyclonic patterns~~ (Fig. 4). In autumn 2018, strong northerly winds only appeared in the northwestern
296 part of study region (Fig. 4a), and were associated with ~~a~~ moderately positive CAI and DA. However,
297 in winter 2018/2019, enhanced northerly winds prevailed almost across the entire study region (Fig.
298 4b), and were associated with ~~an~~ extremely positive CAI and DA. The T_{2m} anomalies averaged over the
299 study region were 3.9 °C in autumn and 0.7 °C in winter (Fig. 4c and 4d), ranking the second and
300 eleventh highest in 1979–2018, respectively.

301 The CHINARE buoys were deployed within a narrow meridional section at about 170° W. On 20
302 August 2018, sea ice concentration in this section, ~~and~~ especially in the southern part, was considerably
303 lower than that in the eastern part of the study region at about 120° W, where other buoys had been
304 deployed (Fig. 5a). Subsequently, ice concentration increased considerably, with almost all buoys being
305 located in the PIZ by 20 September 2018 (Fig. 5b). However, the CHINARE buoys in the south and all
306 T-ICE buoys remained within 70 km ~~of from~~ the ice edge, which retreated further during August–
307 September 2018. By 20 October 2018, ice concentration surrounding all buoys had increased to over
308 95 % (Fig. 5c).

309 In September and early October 2018, ice concentrations were considerably lower than the 1979–2018
310 average. Ice concentrations increased after early October and became comparable with climatological
311 values (Figs. 6b and 7b). In October 2018, ice concentration was much lower in the southern and
312 western parts of the study region compared to the north and east. Subsequently, the spatial gradient of
313 sea ice concentration gradually decreased. Compared ~~to the with~~ 1979–2018 climatology, wind speed
314 ~~over the study period~~ was lower ~~throughout most of the study period during most of the time~~ except for
315 episodic increases as a result of intrusions of low-pressure systems (Figs. 6c and 7c). In September
316 2018, ice speed in the south was higher ~~compared to than that in~~ the north (Fig. 6d), suggesting that the

317 sea ice response to wind forcing was stronger in the south because of the lower ice concentration. From
318 October 2018 onwards, this north–south difference gradually disappeared. The study region was
319 dominated by a low SLP during December 2018 and February 2019, which was related to an
320 anomalously low BH index and subsequent increases in both wind and ice drift speeds (Figs. 6c, 6d, 7c,
321 and 7d).

322 3.2 Spatial and seasonal changes in sea ice kinematic characteristics

323 Temporal resampling has little effect on wind speed. However, applying longer resampling intervals to
324 buoy position data may filter out ice motions that occur at higher frequencies (Haller et al., 2014),
325 resulting in reduced ice speed and IWSR (Fig. 8). For example, ice drift speed and IWSR in September
326 2018 were 0.13 m s⁻¹ and 0.027 at a resampling interval of 1 h, and decreased to 0.01 m s⁻¹ and 0.021
327 at a resampling interval of 48 h. Both ice speed and IWSR decreased considerably from September to
328 November 2018; afterwards, both variables remained low until the end of the study period. At a
329 resampling interval of 6 h, the IWSR was 0.026 in September 2018 (Fig. 8), which is much lower than
330 that (0.013) obtained in the region close to North Pole in the same month of 2007 (Haller et al., 2014)
331 because most parts of our study region included the MIZ at that time. This value decreased to 0.008–
332 0.015 during November to February (Fig. 8), which is comparable to those obtained from the regions
333 north of Siberia or Greenland and the region close to North Pole during the freezing season, but much
334 smaller than that obtained ~~from in~~ Fram Strait (Haller et al., 2014). This implies that, during the
335 freezing season, the response of the sea ice to wind forcing is relatively uniform for the entire Arctic
336 Ocean except for the ~~strait~~-regions close to Fram Strait where ice speeds markedly increases ~~obviously~~.
337 In January 2019, a more consolidated ice pack and a relatively weak wind forcing led to both ice drift
338 speed and IWSR reaching minima for the entire study period (Figs. 6c and 7c). The influence of
339 resampling on the IWSR was ~~considerably~~ reduced considerably during the freezing season, implying
340 significant remarkable reductions of meandering and sub-daily oscillations in ice motion during
341 compared to the meltfreezing season. The ratio between IWSRs at 1-h and 48-h intervals in October
342 was 70 % of that in September ~~and. This ratio~~ remained almost unchanged between November and
343 February.

344 Factors regulating the IWSR are summarized in Table 1. The impact of the geographical location was
345 significant in autumn, with relatively high IWSRs in the southern or western parts of the study region.

346 However, meridional changes in the IWSR became very small in January–February because the north–
347 south gradient in ice conditions was negligible by that time. The west–east gradient was more
348 pronounced, with a significant relationship between longitude and IWSR ~~throughout through~~ the study
349 period. This is consistent with the results given by Lukovich et al. (2011), who identified that the west–
350 east gradient of sea ice motion is larger than that in the north–south direction for the ~~southern south of~~
351 PAO during the freezing season. In summer and early autumn, ~~the~~ consolidation of the ice field is low,
352 and interactions between ~~individual~~ ice floes approximate rigid particle collisions (Lewis and
353 Richter-Menge, 1998). Thus, in August–October 2018, a lower IWSR is related to stronger wind
354 forcing that ~~enhanced the strengthened~~ interactions between floes, which leads to a significant negative
355 statistical correlation between ~~the~~ IWSR and wind speed. Similarly, based on the data obtained from
356 the buoys deployed in the TDS region, Haller et al. (2014) also identified that some spikes of the IWSR
357 tend to be associated with a low wind speed. Consolidation of the ice field between November and
358 February 2018 led to reduced ice motion and weaker sea ice response to wind forcing. Thereby, impact
359 of wind forcing on IWSR was insignificant from November onwards. Variations of T_{2m} across the
360 study region between 20 August and 30 September 2018 were relatively small (–1.7 to –3.5 °C)
361 because of the thermodynamic balance between ~~the~~ sea ice and the atmosphere during the melt season
362 (e.g., Screen and Simmonds, 2010). The statistical relationship between T_{2m} and the IWSR was
363 insignificant during this period. However, the relationship became significant during October–
364 December 2018, with ~~a higher~~ T_{2m} being associated with a ~~higher larger~~ IWSR because warmer
365 conditions may have weakened ice pack (e.g., Oikkonen et al., 2017). As ~~the continuing continued~~
366 thickening of the ice cover further reduced the influence of air temperature on ice kinematics, the
367 statistical relationship between T_{2m} and the IWSR was insignificant in January and February 2019.

368 The initial strength of the inertial oscillation mainly depends on the wind stress. However, the
369 sustainability of ~~the~~ inertial oscillation is restricted by the internal friction within the Ekman ~~ocean~~
370 layer in ~~the region~~s with low ice concentration ~~and much or~~ open waters, or by the ice internal stress in
371 the PIZ (Gimbert et al., 2012). ~~Thus, the~~ inertial component of ice motion is closely associated with
372 the seasonal and spatial changes in ice conditions. Figure 9 shows monthly IMI and PHA obtained
373 from each buoy displayed at the midpoint of the buoy’s trajectory for different months. ~~The combined~~
374 ~~Aa~~verage IMI of all ~~available~~ buoys ~~for the study period~~ was 0.099 ± 0.088 ~~for the entire study period~~,
375 with the average for September 2018 (0.227) being considerably higher. ~~Combined m~~Monthly average

376 IMI_s from all buoys decreased from 0.136 in October 2018 to 0.037 in February 2019. Spatial
377 variability of the IMI had almost disappeared by February 2019; ~~the~~ IMI standard deviation in February
378 2019 was 13 %–22 % of that in September–October 2018. Both the magnitude and the spatiotemporal
379 variations of the PHA were much smaller than those of the IMI. The ~~combined~~ average PHA of all
380 available buoys ~~during the entire study period~~~~for the study period~~ was only 18% of the IMI. The
381 monthly ratio between ~~the~~ PHA and IMI ranged from 0.06 in September 2018 to 0.46 in February 2019.
382 The seasonal damping of this ratio is mainly due to the decrease in the IMI because no statistically
383 significant trend can be identified for the PHA. The standard deviation of the IMI ~~revealed~~ ~~reveals~~ a
384 significant decreasing trend ($P < 0.01$) from 0.069–0.117 in September–October ~~2018~~ to 0.015 in
385 February ~~2019~~, which suggests that the spatial variation of the IMI gradually decreased as ~~the~~ winter
386 ~~approached~~~~approaching~~. Similar ~~to~~ ~~with~~ the ratio between the absolute magnitudes, the ratio between
387 the standard deviations of ~~the~~ PHA and IMI increased from 0.08 in September to 0.50–0.70 in January–
388 February. The seasonal increase in this ratio also was mainly due to the decrease in the standard
389 deviation of the IMI. From comparisons between the seasonalities of ~~the~~ IMI and PHA, we can infer
390 that, the seasonal changes and spatial variations in the IMI could be mainly related to the changes in ~~the~~
391 inertial oscillation, and the contributions of ~~the~~ tidal oscillation can be ignored ~~throughout~~ ~~through~~ the
392 study period.

393 ~~The analysis of the IMI for the entire PAO reveals that its seasonal change mainly occurs in the~~
394 ~~seasonal ice region. On the contrary, that in the pack permanent ice region is almost negligible, which~~
395 ~~implies that the inertial oscillation initialized by wind stress will be attenuated rapidly by the ice~~
396 ~~internal stress in the PIZ regardless of season.~~ To eliminate the influence of large-scale spatial
397 variability, we inspected subsets of data obtained from ~~the buoys that were~~ ~~buoys~~ deployed in clusters.
398 The IMI obtained from the CHINARE buoy cluster (black circles in Fig. 2) decreased markedly from
399 0.223 to 0.081 during September–October 2018. However, a similar change was observed one month
400 later in October–November 2018 for the T-ICE buoy cluster. During the freezing season from
401 November to February, the IMI gradually decreased to 0.038 for the CHINARE cluster and to 0.035 for
402 the T-ICE cluster. Sea ice growth rates_s of the thin ice in the MIZ in the western and southern parts of
403 the study region ~~are~~_s expected to be higher than that in the PIZ in the north or the east (e.g., Kwok and
404 Cunningham, 2008). Accordingly, the spatial variability of ~~the~~ ice inertial oscillation observed in early
405 autumn gradually disappeared.

406 To study the temporal changes in the IMI and PHA in more detail, we used a complex Fourier
407 transformation to obtain time series of the IMI and PHA based on a 5-day temporal window. Here, we
408 only show selected results from three representative buoys for comparison (Fig. 10). Those buoys were
409 initially located in the southernmost and northernmost domain of the CHINARE cluster, and in the
410 southernmost domain of the TICE cluster (Fig. 2). The timing of the seasonal attenuation of the IMI
411 was different between the buoys, occurring in mid-October, late September, and late October 2018 for
412 the CHINARE southernmost and northernmost buoys, and the TICE southernmost buoy, respectively
413 (Fig. 10). During the freezing season, the IMI remained at a low level, but was still always larger than
414 the PHA. The magnitude of the IMI was mainly regulated by wind forcing during the freezing season.
415 The wind speed can significantly explain the magnitude of the IMI in November–February by 22%
416 ($P < 0.05$), 45% ($P < 0.001$), and 21% ($P < 0.05$) for the CHINARE southernmost and northernmost buoys,
417 and the TICE southernmost buoy, respectively. The relatively large wind speed is related to a relatively
418 low IMI because the enhanced wind forcing might increase the ice internal stress and reduce the
419 response of ice motion to inertia forcing. This mechanism is most obvious in the northern PIZ because
420 of the relatively large ice internal stress.

427 **3.3 Spatial and seasonal changes in sea ice deformation**

428 For all ~~the~~ buoy triangles that were used to estimate ice deformation, the ice concentration within the
429 CHINARE buoy cluster increased most rapidly during late August and early September 2018, and it
430 remained close to 100 % from then onwards (Fig. ~~40a11a~~). ~~However, a~~ comparable seasonal increase
431 in ice concentration ~~within the TICE buoy cluster~~ was observed within the TICE buoy cluster one
432 month later. To facilitate a direct comparison of the data obtained by the two different ~~from two~~ buoy
433 clusters, we estimated the ice deformation rate of the T-ICE buoy cluster at the 10–20 km scale using
434 the value at the 40–80 km scale and a constant spatial scaling exponent of 0.55. The scaling exponent
435 of 0.55 is a seasonal average obtained from the CHINARE buoy cluster. A change of the scaling
436 exponent by 10 % would lead to an uncertainty of about 0.03 for the ice deformation rate. Thus, a
437 constant scaling exponent can be considered acceptable for a study of seasonal variation. In early and
438 mid-September 2018, the ice deformation rate was low for the CHINARE cluster (Fig. ~~40b11b~~)
439 because of low and relatively stable wind ~~forcingspeed and relatively stable wind direction, and despite~~
440 a weakly consolidated ice field (Fig. 2). For the ~~TICET-ICE~~ cluster, both ice deformation rate and ratio

441 between ice deformation rate and wind speed decreased rapidly between 20 September and 10
442 November 2018, associated with [a](#) consolidation of the ice field as ice concentration and thickness
443 increased, and temperature decreased. However, [the](#) ice deformation rate [obtained by from](#) the
444 CHINARE [buoy](#) cluster decreased only slightly over the same period, which is likely [linked to its](#)
445 [relatively low](#) ~~because its~~ initial deformation rate ~~was relatively low~~ in late September 2018, and
446 ~~associated with~~ [to](#) the higher ice concentration (15 %–20 %) ~~compared to in the CHINARE region~~
447 ~~than that in~~ the T-ICE region ~~by 15 %–20 %~~.

448 For the CHINARE buoy cluster, [the](#) daily wind speed can explain 35 % ($P < 0.001$) of the daily ice
449 deformation rate estimated ~~from using~~ hourly position data [throughout over](#) the study period. However,
450 for the T-ICE cluster, changes in ice deformation were mainly regulated by the seasonal evolution of
451 ice concentration between September and early November 2018. The relationship between ice
452 deformation rate and wind speed was insignificant at the statistical confidence level of 0.05 during this
453 period. The ice field had sufficiently consolidated by mid-November 2018, and the relationship
454 between daily ice deformation rate and daily wind speed changed to significant ($R^2 = 0.12$, $P < 0.01$)
455 from then onwards.

456 The average ratio of ice deformation rate to wind speed in autumn was $1.15 \times 10^{-6} \text{ m}^{-1}$ for the
457 CHINARE cluster and $0.62 \times 10^{-6} \text{ m}^{-1}$ for the T-ICE cluster; the ratio in winter decreased to 0.86×10^{-6}
458 and $0.17 \times 10^{-6} \text{ m}^{-1}$, respectively. This [seasonal pattern](#) is consistent with results of Spreen et al. (2017),
459 who used the RGPS data to reveal that the annual maximum ice deformation rate occurred in August,
460 and decreased gradually to the annual minimum in March. Except for late September 2018, when [the](#)
461 ice concentration in the T-ICE cluster was less than 85 %, [the](#) ice deformation rate from the CHINARE
462 cluster was generally larger than that ~~from of~~ the T-ICE cluster, with average values of 0.45 and 0.13
463 d^{-1} , respectively, for October 2018 to February 2019. Sea ice in the region of the T-ICE cluster was
464 generally thinner [compared to than that in](#) the region of the CHINARE cluster. Thus, the difference in
465 ice deformation rate cannot be explained by [a](#) difference ~~of in~~ ice conditions between the two regions,
466 and is most likely related to [the](#) spatial heterogeneity of wind and/or oceanic forcing. Changes in the
467 direction of wind vectors were more frequent around the CHINARE cluster than around the T-ICE
468 cluster. Frequent changes in ice drift direction lead to larger ice deformation [events](#), such as ~~those the~~
469 ~~events~~ on 11 October, and 11 and 26 November 2018 for the CHINARE cluster as shown in Fig.
470 ~~10b11b~~. The drifting trajectories of the T-ICE cluster were much straighter than those of the

471 CHINARE cluster. ~~Since t-~~ Furthermore, the CHINARE cluster was located in the core region of the
472 BG; ~~thus, the~~ vorticity of the surface current must be greater than that in the T-ICE cluster, ~~which was~~
473 located at the western boundary of the BG (Armitage et al., 2017). As a result, ice deformation rate and
474 its ratio to wind speed were lower for the T-ICE cluster ~~than for CHINARE cluster~~.

475 Ice deformation rates obtained from the CHINARE buoy cluster at three representative lengths of 7.5,
476 15, and 30 km were estimated using Eq. (6). Figure ~~11-12~~ shows that ~~the~~ monthly average ice
477 deformation decreased as ~~the~~ length scale and resampling interval increased, implying ~~an ice~~
478 deformation localization and intermittency. ~~The i~~Ice deformation decreased rapidly at all spatial and
479 temporal scales during the seasonal transition period of September–October, and remained low from
480 then onwards. Ice deformation rate obtained using hourly position data from the CHINARE buoy
481 cluster in September 2018 was 0.38 d^{-1} at the length scale of 30 km, which is comparable ~~with-to~~ that
482 in September 2016 (0.31 d^{-1}), and much larger than that in September 2014 (0.18 d^{-1}) observed also in
483 northern PAO (Lei et al., 2020b). These observed differences can be related to the strong storms in late
484 September 2018 (Fig. ~~10b11b~~) and early September 2016 (Lei et al., 2020b), in contrast to the
485 relatively stable synoptic conditions and relatively compact ice conditions in September 2014 (Lei et
486 al., 2020b).

487 Accordingly, the spatial scaling exponent β estimated from hourly position data was 0.61 in September
488 2018, ~~which and~~ is comparable ~~to β with that~~ from September 2016 (0.60), but slightly larger than
489 ~~that~~ in September 2014 (0.46) observed in northern PAO (Lei et al., 2020b). ~~The value of β~~ decreased
490 markedly from September to October 2018, and varied little from then onwards (Fig. ~~1213~~). With
491 ~~increasinges~~ in ice thickness and concentration ~~as well as a and~~ cooling of the ice cover from October
492 onwards, ~~the~~ consolidation of the ice field is enhanced, and sea ice deformation can spread over longer
493 distances. By February 2019, ~~the spatial scaling exponent β obtained~~ from hourly position data
494 decreased to 0.48, which is comparable ~~with-to that (0.43) obtained from~~ February 2015 (~~0.43~~) in the
495 northern PAO (Lei et al., 2020a). This suggests that the ~~interannual year-to-year~~ changes in the spatial
496 scaling of ice deformation during winter are not as strong as that in early autumn, which is in line with
497 the ~~evolution change pattern~~ of ice thickness (e.g., Kwok and Cunningham, 2008). ~~The value of β~~
498 decreased exponentially with ~~an the~~ increase in ~~re~~sampling frequency for all months, which indicates
499 ~~that~~ the spatial scaling would ~~generally~~ be underestimated ~~when using data of coarser with the~~

500 ~~observations of coarsened temporal resolution. The β i~~Interpolated to 3 h, β was 0.42 and 0.44 in
501 January and February 2019, respectively, which is comparable with ~~the result that~~ (0.40) obtained from
502 ~~the~~ south of the PAO during March–May (Itkin et al., 2017). The ice growth season generally lasts ~~to~~
503 ~~until~~ May–June in the PAO (Perovich et al., 2003), which implies ~~that the sea ice~~ the consolidation ~~of~~
504 ~~sea ice~~ in March–May is comparable to, or even stronger than, that in January–February. Thus, ~~our the~~
505 ~~β derived from our results~~ is essentially consistent with that given by Itkin et al. (2017). ~~The β~~
506 ~~e~~Extrapolated to 48 h (120 h), β decreased to 0.29 (0.25) in January and 0.33 (0.28) in February 2019,
507 respectively, which ~~is was~~ comparable to that (0.20) obtained from the estimations using RADARSAT
508 images with temporal resolution of 48–120 h during the freezing season for the ~~pan-pan~~-Arctic Ocean
509 (Stern and Lindsay, 2009). We further use the seasonal bin to test the sensitivity of the estimation of β to
510 the number of samples. Consequentially, the seasonal β was estimated at 0.54 and 0.48 for autumn and
511 winter, respectively, which is close to those (0.53 and 0.49) averaged directly from the monthly values.
512 Therefore, we believe that the monthly segmentation for estimations of β is statistically appropriate and
513 can better reveal seasonal changes.

514 The temporal scaling exponent α also exhibited a strong dependence on the spatial scale, which means
515 ~~a~~ relatively large intermittency of ice deformation can be obtained by fine-scale observations (Fig.
516 ~~4314~~). Seasonally, the value of α decreased between September and October 2018 because of enhanced
517 consolidation of the ice cover. The value of the space–time coupling coefficient c increased
518 monotonously from 0.034 in autumn to 0.062 in winter, suggesting ~~a~~ gradual enhancement of the brittle
519 rheology of the ice cover. This is consistent with the results derived from RADARSAT images (Stern
520 and Moritz, 2002), which revealed that sea ice deformation is more linear in winter, and more clustered
521 and spatially random in summer. The value of c in September 2018 is comparable ~~with to~~ that in
522 September 2016 (0.03). However, it is only about half that in September 2014 (0.06) (Lei et al., 2020b)
523 because of the different ice conditions. The value of c in January–February 2019 (0.059–0.062) is
524 comparable with the values obtained in January–February 2015 (0.051–0.077) from the northern PAO
525 (Lei et al., 2020a), and the value obtained from the region north of Svalbard in winter and spring
526 (Oikkonen et al., 2017).

527 The areal localization index denotes the area with the highest ~~(15%)~~ deformation. It had a strong
528 dependence on the temporal scale, and increased linearly ($P < 0.001$) as the logarithm of the temporal

529 scale increased (Fig. 4415), which implies that the localization of ice deformation would be
530 underestimated ~~when using coarser temporal by the observations or models with coarser~~ resolution.
531 Seasonally, the areal localization index decreased ~~significantly remarkably~~ from September to
532 November 2018, indicating that ice deformation was increasingly localized during the transition from
533 melting to freezing. During the freezing season, ~~the~~ ice deformation mainly occurs along linear cracks,
534 leads, and/or ridges, which ~~corresponds is related~~ to a high localization; ~~While~~ during melt season, the
535 ice deforming zones are in clumps rather than along lines, ~~and~~ ~~the~~ The spatial distribution of ice
536 deformation rate is more even and amorphous (Stern and Moritz, 2002), which ~~corresponds, which is~~
537 ~~related~~ to a low localization. During freezing season from November to February, the degree of
538 deformation strongly regulated the localization of ice deformation, with the monthly ice deformation
539 rate explaining 96 % of the monthly areal localization index ($P < 0.01$). This means that ~~an~~ extremely
540 high ice deformation can spread over longer distances. The areal localization index for January–
541 February 2019 corresponding to a temporal resolution of 1 h and a length scale of 10–20 km was
542 1.9 %–2.3 %. ~~This is, which was~~ close to ~~the values (1.6%)~~ estimated ~~using RADARSAT images at a~~
543 ~~scale of 13–20 km (1.6%) (Marsan et al., 2004) and at a scale of 10 km (1.5%) (Stern and Lindsay,~~
544 ~~2009) at scale of 13–20 km (Marsan et al., 2004), and that (1.5%) at a scale of 10 km (Stern and~~
545 ~~Lindsay, 2009) using RADARSAT images, as well as that (2.4 %–2.7 %) estimated at a scale of 18 km~~
546 using a high resolution numerical model (2.4 %–2.7 %) (Spreen et al., 2017). We ~~also analyzed further~~
547 ~~analyze~~ other fractional areas accommodating the largest 10 % or 20 % of the ice deformation.
548 Although the adjusted indices would have different magnitudes, their ~~overall seasonal patterns of~~
549 ~~seasonal change~~ and ~~the~~ dependence on the temporal scale are consistent ~~with as~~ those ~~obtained~~ using
550 the threshold of 15%. ~~We therefore conclude that~~ ~~Therefore~~, the understanding of the ice deformation
551 localization derived from this study is not very sensitive to the selected threshold.

552 3.4 Spatial differences in the trends of sea ice loss in the PAO and their implications for sea ice 553 kinematics and deformation

554 Sea ice conditions in the melt season have profound effects on sea ice dynamic and thermodynamic
555 processes in the following winters. For example, enhanced divergence of summer sea ice leads to
556 increased absorption of solar radiation by the upper ocean and delays onset of ice growth (e.g., Lei et
557 al., 2020b). As shown in Fig. 4516, the long-term decrease of sea ice concentration in the first half of

558 September, when Arctic sea ice extent [typically](#) reaches its annual minimum (Comiso et al., 2017), is
559 stronger in the southern and western parts of the study region than in the north and the east. The
560 western and southern parts of the study region have become ice free in September during recent years.
561 On the contrary, there is no significant trend in ice concentration in the first half of September along
562 the trajectory of the easternmost buoy (Fig. ~~45e16e~~). This suggests that, the melting period is getting
563 longer in the southern and western ~~parts of the~~ PAO compared to the [northern and eastern PAO](#)~~north-~~
564 ~~and east~~. Consequently, the spatial gradient of ice thickness in the PAO, especially during autumn and
565 early winter, will be further enhanced ~~by the delay in sea ice freezing onset and reduced through~~
566 ~~delaying the onset of ice growth and reducing~~ ice thickness in the south and west. [A deformation of the](#)
567 [ice field in the seasonal ice zone creates unfrozen ice ridges \(Salganik et al., 2020\). These new ridges,](#)
568 [together with the newly formed thin ice in leads, are mechanically vulnerable components of the ice](#)
569 [field during the freezing season, and predispose the ice field to further deformation under external](#)
570 [forces](#). At the end of the freezing season, the enhanced ice deformation will promote the sea ice
571 breaking up and expand the MIZ northward, which is conducive to the advance of the melt season.
572 Thus, the north–south and east–west differences in sea ice kinematics are likely to be more pronounced
573 in the future.

574 **4 Conclusion and outlook**

575 High-resolution position data recorded by 32 ice-based drifting buoys in the PAO between August
576 2018 and February 2019 were analyzed in detail to characterize spatiotemporal variations of sea ice
577 kinematic and deformation properties. During the transition from autumn to winter, ice deformation
578 and its response to wind forcing, as well as the inertial signal of ice motion gradually weakened. At the
579 same time, space–time coupling of ice deformation was enhanced as the mechanical strength of the ice
580 field increased. ~~After a complex Fourier transformation, we found that t~~The influence of tidal forcing
581 on the quasi-semidiurnal oscillation of ice motion was negligible regardless of [the](#) season because the
582 buoys drifted over [the](#) deep [basins waters](#) beyond the continental shelf. During the freezing season
583 between October 2018 and February 2019, [the](#) ice deformation rate in the northern part of the study
584 region was about 2.5 [higher compared to times that](#) in the western part. This difference is likely related
585 to the higher spatial heterogeneity of the oceanic and atmospheric forcing in the northern part of the

586 study region, which ~~is situated lies~~ in the core region of the BG. Because of ~~the~~ seasonal change in the
587 large-scale atmospheric circulation pattern, ~~indicated by especially for~~ the enhanced positive phases of
588 the CAI and DA, a significant change in ice drift direction from anticyclonic to cyclonic patterns was
589 observed in late November 2018, leading to temporal increases in both ice deformation rate and its
590 ratio to wind forcing.

591 The pronounced high intermittence of ice deformation suggests that an episodic opening or closing of
592 the sea ice cover may be undetectable from data with longer sampling intervals, such as remote sensing
593 data with resolutions of one or two days. Consequently, fluxes of heat (e.g., Heil and Hibler, 2002) or
594 particles and gases (e.g., Held et al., 2011) released from these openings in the PIZ ~~into~~ the atmosphere
595 would be underestimated if they are derived from ~~remote sensing products such data~~. The dependence
596 of the ratio of ice speed to wind speed on resampling frequency also suggests that ~~the~~ temporal
597 resolution should be considered carefully when using ~~reanalyzed~~ wind data to parameterize or simulate
598 sea ice drift. From a spatial perspective, our results reveal that ice deformation intermittence is
599 underestimated at longer scales. This is consistent with results from numerical models, which indicate
600 that the most extreme deformation events may be absent in the output of models with lower spatial
601 resolution (Rampal et al., 2019). This emphasizes the need for high-resolution sea ice dynamic models
602 (e.g., Hutter and Losch, 2020) to reproduce linear kinematic features of ice deformation.

603 The response of ice kinematics to wind and inertia forcing was stronger in the south and west compared
604 to the north and east of the study region, which is partly associated with the spatial heterogeneity of ice
605 conditions inherited from previous seasons. During the transition from autumn to winter, the north–
606 south and east–west gradients in the IWSR and ~~the~~ inertial component of ice motion gradually
607 decreased and even disappeared entirely, which is in line with the seasonal evolution of ice
608 concentration and thickness. ~~The spatial Spatial~~ heterogeneity in ~~autumn~~ ice conditions ~~in autumn~~ is
609 likely to be amplified with ~~an~~ increased loss of summer ~~sea~~ ice cover in the southern and western ~~parts~~
610 ~~of the~~ PAO, which is expected to further enhance the east-west and north-south differences in sea ice
611 kinematics.

612 We conclude this study by highlighting some of the most important knowledge gaps related to sea ice
613 kinematics and deformation in the Arctic Ocean, not necessarily limited to the PAO, and how they can
614 be addressed in the future. First, the spatio-temporal scale effects of ice deformation in this study were

615 derived based on data recorded by buoys distributed over spatial scales of only 5–40 km. In order to
616 assess whether the results of the present study are also representative for a much larger domain,
617 observations by a much wider and denser buoy array, ideally combined with high-resolution ship-based
618 radar and satellite remote sensing data, as well as the support of numerical models, are needed. Second,
619 we only examined atmospheric influences on sea ice kinematics and deformation. The ocean also plays
620 an important role on ice drift and deformation, especially on mesoscales, greatly enhancing ice motion
621 nonuniformity and ice deformation (e.g., Zhang et al., 1999). In the PAO, mesoscale eddies prevail
622 over the shelf break and the Northwind and Alpha-Mendeleyev Ridges (e.g., Zhang et al., 1999, Zhao
623 et al., 2016). To assess the influence of mesoscale oceanic eddies on ice deformation, observations
624 from ice-drifter arrays are insufficient, highlighting the need for a complementary deployment of
625 ocean-profiler arrays. Third, deformation of sea ice creates ample opportunity for increased sea ice
626 biological activities. Irradiance and nutrients, the two major limiting agents for biological growth in the
627 sea ice realm (Ackley and Sullivan, 1994), are strongly impacted by sea ice deformation. For example,
628 pressure ridges generally have large semi-enclosed chambers, which can provide more nutrients for
629 biological activity (Ackley and Sullivan, 1994; Geiger and Perovich, et al., 2008). Sea ice deformation
630 would also increase ice surface roughness, which in turn increases the potential of melt pond formation
631 in early summer (e.g., Perovich and Polashenski, 2012). The formation of ponds leads to an increase in
632 the transmission of irradiance through the ice cover and promote the biological growth (e.g., Nicolaus
633 et al., 2012). In order to better understand the linkages between sea ice dynamical and biological
634 processes, more joint observations are urgently needed.

635 In September 2019, the international Multidisciplinary drifting Observatory for the Study of Arctic
636 Climate (MOSAiC) drift experiment (2019–2020) was launched in the region north of the Laptev Sea
637 (Krumpen et al., 2020), which is to the west of the deployment region of the TICE buoy cluster. The
638 ice thickness around the MOSAiC ice station was much lower than that in the areas of the buoy clusters
639 included in this study (Krumpen et al., 2020). Frequent sea ice breakup events have been reported
640 around the MOSAiC ice camp during the drift. An integral part of MOSAiC was the deployment of a
641 large Distributed Network of ice-based drifting buoys of various types around the main ice camp.
642 Supported by a wealth of multi-disciplinary in-situ data, satellite remote sensing data and numerical
643 model setups, MOSAiC has the potential to properly address all the aspects outlined above. At the

644 same time, data and results from the present study can be used as a proxy baseline for comparing and
645 investigating deformation of the MOSAiC ice pack. By comparing our results to the observations from
646 the MOSAiC buoy array, we may get a broader understanding of the spatial variation of Arctic sea ice
647 deformation.

648 ~~Multi year ice in the Pacific and eastern sectors of the Arctic Ocean is being gradually depleted~~
649 ~~(Serreze and Meier, 2018), resulting in the domination of seasonal sea ice. Consequently, a~~
650 ~~deformation of the ice field in this region creates unfrozen first year ice ridges (Salganik et al., 2020).~~
651 ~~These new ridges, together with the newly formed thin ice in leads, are mechanically vulnerable~~
652 ~~components of the ice field, and predispose the ice field to further deformation under external forces.~~
653 ~~The international Multidisciplinary drifting Observatory for the Study of Arctic Climate (MOSAiC)~~
654 ~~drift experiment (2019–2020) started from the region north of the Laptev Sea (Krumpen et al., 2020),~~
655 ~~which is to the west of the T-ICE buoy cluster. Ice thickness around the MOSAiC ice station was much~~
656 ~~lower (Krumpen et al., 2020) than that in the areas of the buoy clusters included in this study. Frequent~~
657 ~~sea ice breaking has been observed around the central observatory of MOSAiC during the drift. Data~~
658 ~~and results from the present study can be used as a proxy baseline for comparing and investigating~~
659 ~~deformation of the MOSAiC ice pack. By comparing our results to the observations from the MOSAiC~~
660 ~~buoy array, we may get a broader understanding of the spatial variation of sea ice deformation over the~~
661 ~~pan-Arctic Ocean.~~

662 ~~In this study, we only examined atmospheric influences on sea ice kinematics and deformation. The~~
663 ~~ocean also plays an important role on ice drift and deformation, especially on mesoscales, greatly~~
664 ~~enhancing ice motion nonuniformity and ice deformation (e.g., Zhang et al., 1999). In the PAO,~~
665 ~~mesoscale eddies prevail over the shelf break and the Northwind and Alpha Mendeleev Ridges (e.g.,~~
666 ~~Zhang et al., 1999, Zhao et al., 2016). To assess the influence of mesoscale oceanic eddies on ice~~
667 ~~deformation, observations from ice drifter arrays are insufficient. This highlights the need for a~~
668 ~~complementary deployment of ocean profiler arrays, which was for example realized recently as part~~
669 ~~of the distributed network of MOSAiC (Krumpen et al., 2020).~~

670 ~~Deformation of sea ice creates ample opportunity for increased sea ice biological activities. Irradiance~~
671 ~~and nutrients, the two major limiting agents for biological growth in the sea ice realm (Ackley and~~
672 ~~Sullivan, 1994), are strongly impacted by sea ice deformation. For example, pressure ridges generally~~

673 ~~have large semi-enclosed chambers, which can provide more nutrients for biological activity (Ackley~~
674 ~~and Sullivan, 1994; Geiger and Perovich, et al., 2008). Sea ice deformation would also increase ice~~
675 ~~surface roughness, which in turn increases the potential of melt pond formation in early summer (e.g.,~~
676 ~~Perovich and Polashenski, 2012). The formation of ponds leads to an increase in the transmission of~~
677 ~~irradiance through the ice cover and promote the biological growth (e.g., Nicolaus et al., 2012). In~~
678 ~~order to better understand the linkages between sea ice dynamical and biological processes, more joint~~
679 ~~observations are urgently needed.~~

680 **Author contributions**

681 RL is responsible for project coordination and paper writing. MH, BC, GZ, and GD undertook the
682 processing and analysis of the buoy data, and interpretation of results. RL, WY, and JB deployed the
683 buoys. The buoy data were provided by RL, MH, and BC. The atmospheric circulation index was
684 calculated by QC. All authors commented on the manuscript.

685 **Data availability**

686 The CHINARE buoy data are archived in the National Arctic and Antarctic Data Centre of China at
687 <https://www.chinare.org.cn/metadata/53de02c5-4524-4be4-b7bb-b56386f1341c> (DOI:
688 10.11856/NNS.D.2020.038.v0). The TICE buoy data are available for download in the online sea-ice
689 knowledge and data platform www.meereisportal.de and will be archived in PANGAEA. The IABP
690 buoy data are archived at <http://iabp.apl.washington.edu/index.html>.

691 **Competing interests**

692 The authors declare that they have no conflict of interest.

693 **Acknowledgments**

694 We are most grateful to the Chinese Arctic and Antarctic Administration and the
695 Alfred-Wegener-Institute for their logistical and financial support of the cruises of CHINARE and
696 T-ICE, respectively. We thank the captains, crews and science parties of the R/V Xuelong and the
697 Akademik Tryoshnikov, especially cruise leaders Dr. Zexun Wei and Dr. Benjamin Rabe, for their

698 incredible support during the expeditions. The AMSR2 passive microwave ice concentrations were
699 provided by the University of Bremen. The SMMR-SSMIS ice concentration and ice motion products,
700 and the monthly Arctic Sea Ice Index were provided by the NSIDC. The ERA-Interim reanalysis was
701 obtained from the ECMWF. Monthly sea level pressure is obtained from the NCEP/NCAR reanalysis I
702 dataset. We are very grateful to the two anonymous reviewers and the responsible editor Dr. Ted
703 Maksym for their comments, which have greatly improved our paper.

704 **Financial support**

705 This work was supported by grants from the National Key Research and Development Program
706 (2016YFC1400303, 2018YFA0605903, and 2016YFC1401800) and the National Natural Science
707 Foundation of China (41722605 and 41976219). B.C. was supported by the European Union's Horizon
708 2020 research and innovation programme (727890 – INTAROS) and Academy of Finland under contract
709 317999. The buoys deployed on T-ICE were funded by the Alfred-Wegener-Institute through the
710 infrastructure programs FRAM and ACROSS.

711 **References**

- 712 Ackley, S.F., Sullivan, C.W.: Physical controls on the development and characteristics of Antarctic sea
713 ice biological communities—a review and synthesis, *Deep-Sea Research I* 41 (10), 1583–1604,
714 1994.
- 715 Alam, A. and Curry, J. A.: Evolution of new ice and turbulent fluxes over freezing winter leads, *J.*
716 *Geophys. Res. Oceans*, 103, 15783–15802, 1998.
- 717 Armitage, T. W. K., Bacon, S., Ridout, A. L., Petty, A. A., Wolbach, S., and Tsamados, M.: Arctic Ocean
718 surface geostrophic circulation 2003–2014, *The Cryosphere*, 11, 1767–1780,
719 <https://doi.org/10.5194/tc-11-1767-2017>, 2017.
- 720 Assmy, P., Fernández-Méndez, M., Duarte, P., and other coauthors: Leads in Arctic pack ice enable early
721 phytoplankton blooms below snow-covered sea ice, *Sci. Rep.*, 7:40850.
722 <https://doi.org/10.1038/srep40850>, 2017.

723 Bi, H., Yang, Q., Liang, X., Zhang, L., Wang, Y., Liang, Y., and Huang, H.: Contributions of advection
724 and melting processes to the decline in sea ice in the Pacific sector of the Arctic Ocean., *The*
725 *Cryosphere*, 13, 1423–1439, <https://doi.org/10.5194/tc-13-1423-2019>, 2019.

726 Geiger C. A., and Perovich D. K.: Springtime ice motion in the western Antarctic Peninsula region,
727 *Deep-Sea Res. II*, 55, 338–350, 2008.

728 Comiso, J. C., Meier, W. N., and Gersten, R.: Variability and trends in the Arctic sea ice cover: results
729 from different techniques, *J. Geophys. Res. Oceans*, 122, 6883–6900, doi:10.1002/2017JC012768, ,
730 2017.

731 Dee, D. P., Uppala, S. M., Simmons, A. J., et al.: The ERA-interim reanalysis: configuration and
732 performance of the data assimilation system, *Quarterly Journal of the Royal Meteorological Society*,
733 137, 553–597. <https://doi.org/10.1002/qj.828>, 2011.

734 Ding, Q., Schweiger, A., L’Heureux, M., Battisti, D. S., Po-Chedley, S., Johnson, N. C.,
735 Blanchard-Wrigglesworth, E., Harnos, K., Zhang, Q., Eastman, R., and Steig, E. J.: Influence of
736 high-latitude atmospheric circulation changes on summertime Arctic sea ice, *Nature Clim*
737 *Change*, 7, 289–295, 2017.

738 Fetterer, F., Knowles, K., Meier, W. N., Savoie, M., and Windnagel, A. K.: Updated daily sea ice index,
739 version 3, sea ice concentration, Boulder, Colorado USA. NSIDC: National Snow and Ice Data
740 Center. doi: <https://doi.org/10.7265/N5K072F8>, 2017.

741 Fernández-Méndez, M., Olsen, L. M., Kauko, H. M., and other coauthors: Algal hot spots in a changing
742 Arctic Ocean: sea-ice ridges and the snow-ice interface, *Front Mar. Sci.*, 5: 75.
743 <https://doi.org/10.3389/fmars.2018.00075>, 2018.

744 Gimbert, F., Marsan, D., Weiss, J., Jourdain, N. C., and Barnier, B.: Sea ice inertial oscillations in the
745 Arctic Basin, *The Cryosphere*, 6, 1187–1201, 2012.

746 Haller, M., Brümmer, B., and Müller, G.: Atmosphere–ice forcing in the transpolar drift stream: results
747 from the DAMOCLES ice-buoy campaigns 2007–2009, *The Cryosphere*, 8, 275–288, 2014.

748 Heil, P., and Hibler III, W. D.: Modeling the high-frequency component of Arctic sea ice drift and
749 deformation, *J. Phys. Oceanogr.*, 32, 3039–3057, 2002.

750 Held, A., Brooks, I. M., Leck, C., and Tjernström M.: On the potential contribution of open lead particle
751 emissions to the central Arctic aerosol concentration, *Atmos. Chem. Phys.*, 11, 3093–3105,
752 <https://doi.org/10.5194/acp-11-3093-2011>, 2011.

753 Herman, A., and Glowacki, O.: Variability of sea ice deformation rates in the Arctic and their
754 relationship with basin-scale wind forcing, *The Cryosphere*, 6(6), 1553–1559,
755 doi:10.5194/tc-6-1553-2012, 2012.

756 Hutchings, J. K., and Hibler III, W. D.: Small-scale sea ice deformation in the Beaufort Sea seasonal ice
757 zone, *J. Geophys. Res.*, 113, C08032, doi:10.1029/2006JC003971, 2008.

758 Hutchings, J. K., Heil, P., Steer, A., and Hibler III, W. D.: Subsynoptic scale spatial variability of sea ice
759 deformation in the western Weddell Sea during early summer, *J. Geophys. Res.*, 117, C01002,
760 doi:10.1029/2011JC006961, 2012.

761 Hutchings, J. K., Roberts, A., Geiger, C. A., and Richter-Menge, J.: Spatial and temporal
762 characterization of sea-ice deformation, *Ann. Glaciol.*, 52(57), 360–368, 2011.

763 Hutchings, J. K., Roberts, A., Geiger, C. A., and Richter-Menge, J.: Corrigendum: Spatial and temporal
764 characterization of sea-ice deformation, *J. Glaciol.*, 64(244), 343–346, 2018.

765 Hutter, N., Losch, M., and Menemenlis, D.: Scaling properties of arctic sea ice deformation in a
766 high-resolution viscous-plastic sea ice model and in satellite observations, *J. Geophys. Res. Oceans*,
767 123, 672–687, <https://doi.org/10.1002/2017JC013119>, 2018.

768 Hutter, N., and Losch, M.: Feature-based comparison of sea ice deformation in lead-permitting sea ice
769 simulations, *The Cryosphere*, 14, 93–113, <https://doi.org/10.5194/tc-14-93-2020>, 2020.

770 Itkin, P., Spreen, G., Cheng, B., Doble, M., Girard-Arduin, F., Haapala, J., Hughes, N., Kaleschke, L.,
771 Nicolaus, M., and Wilkinson, J.: Thin ice and storms: Sea ice deformation from buoy arrays deployed
772 during N-ICE2015, *J. Geophys. Res.*, 122, 4661–4674, doi:10.1002/2016JC012403, 2017.

773 Itkin, P., Spreen, G., Hvidegaard, S. M., Skourup, H., Wilkinson, J., Gerland, S., and Granskog, M. A.:
774 Contribution of deformation to sea ice mass balance: A case study from an N-ICE2015 storm,
775 *Geophys. Res. Lett.*, 45, 789–796, <https://doi.org/10.1002/2017GL076056>, 2018.

776 [Kowalik, Z., and Proshutinsky, A. Y.: Diurnal tides in the Arctic Ocean, *J. Geophys.*](#)
777 [Res., 98\(C9\), 16449– 16468, doi:10.1029/93JC01363, 1993.](#)

778 Krumpen, T., Birrien, F., Kauker, F., and other coauthors: The MOSAiC ice floe: sediment-laden
779 survivor from the Siberian shelf, *The Cryosphere*, 14, 2173–2187,
780 <https://doi.org/10.5194/tc-14-2173-2020>, 2020.

781 Kwok, R.: Contrasts in sea ice deformation and production in the Arctic seasonal and perennial ice zones,
782 *J. Geophys. Res.*, 111, C11S22, doi:10.1029/2005JC003246, 2006.

783 Kwok, R., and Cunningham, G. F.: ICESat over Arctic sea ice: Estimation of snow depth and ice
784 thickness, *J. Geophys. Res.*, 113, C08010, doi:10.1029/2008JC004753, 2008.

785 Lammert, A., Brümmer, B., and Kaleschke, L.: Observation of cyclone-induced inertial sea-ice
786 oscillation in Fram Strait, *Geophys. Res. Lett.*, 36, L10503, doi:10.1029/2009GL037197, 2009.

787 Lei, R., Tian-Kunze, X., Leppäranta, M., Wang, J., Kaleschke, L., and Zhang Z.: Changes in summer sea
788 ice, albedo, and partitioning of surface solar radiation in the Pacific sector of Arctic Ocean during
789 1982–2009, *J. Geophys. Res. Oceans*, 121, 5470–5486, doi:10.1002/2016JC011831, 2016.

790 Lei, R., Gui, D., Hutchings, J. K., Wang, J., Pang X.: Backward and forward drift trajectories of sea ice in
791 the northwestern Arctic Ocean in response to changing atmospheric circulation. *Int. J. Climatol.*, 1–
792 20. DOI: 10.1002/joc.6080, 2019.

793 Lei, R., Gui, D., Hutchings, J. K., Heil, P., Li, N.: Annual cycles of sea ice motion and deformation
794 derived from buoy measurements in the western Arctic Ocean over two ice seasons. *J. Geophys. Res.*,
795 125, e2019JC015310, <https://doi.org/10.1029/2019JC015310>, 2020a.

796 Lei, R., Gui, D., Heil, P., Hutchings, J.K., Ding, M.: Comparisons of sea ice motion and deformation, and
797 their responses to ice conditions and cyclonic activity in the western Arctic Ocean between two
798 summers, *Cold Reg. Sci. Technol.*, 170, 102925, <https://doi.org/10.1016/j.coldregions.2019.102925>,
799 2020b.

800 Lewis, J. K., and Richter-Menge, J. A.: Motion-induced stresses in pack ice, *J. Geophys.*
801 *Res.*, 103(C10), 21831–21843, doi:10.1029/98JC01262, 1998.

802 Lindell, D. B., and Long, D. G.: Multiyear Arctic ice classification using ASCAT and SSMIS. *Remote*
803 *Sens.*, 8, 294; doi:10.3390/rs8040294, 2016.

804 Lukovich, J. V., Babb, D. G., and Barber D. G.: On the scaling laws derived from ice beacon trajectories
805 in the southern Beaufort Sea during the International Polar Year-Circumpolar Flaw Lead study,
806 2007–2008, *J. Geophys. Res.*, 116, C00G07, doi:10.1029/2011JC007049, 2011.

807 Marsan, D., Stern, H., Lindsay, R., and Weiss, J.: Scale dependence and localization of the deformation
808 of Arctic sea ice, *Phys. Res. Lett.*, 93, 17, 178501, doi:10.1103/PhysRevLett.93.178501, 2004.

809 Marsan, D., and Weiss, J.: Space/time coupling in brittle deformation at geophysical scales, *Earth Planet*
810 *Sci. Lett.*, 296(3–4), 353–359, 2010.

811 Moore, G. W. K., Schweiger, A., Zhang, J., and Steele, M.: Collapse of the 2017 winter Beaufort High: A
812 response to thinning sea ice? *Geophys. Res. Lett.*, 45: 2860–2869.
813 <https://doi.org/10.1002/2017GL076446>, 2018.

814 Nicolaus, M., Katlein, C., Maslanik, J., and Hendricks, S.: Changes in Arctic sea ice result in increasing
815 light transmittance and absorption, *Geophys. Res. Lett.*, 39, L24501, doi:10.1029/2012GL053738,
816 2012

817 Oikkonen, A., Haapala, J., Lensu, M., Karvonen, J., and Itkin, P.: Small-scale sea ice deformation during
818 N-ICE2015: From compact pack ice to marginal ice zone, *J. Geophys. Res. Oceans*, 122, 5105–5120,
819 doi:10.1002/2016JC012387, 2017.

820 Perovich, D. K., Grenfell, T. C., Richter-Menge, J. A., Light, B., Tucker III, W. B., and Eicken, H.: Thin
821 and thinner: sea ice mass balance measurements during SHEBA, *J. Geophys. Res.*, 108(C3), 8050,
822 doi:10.1029/2001JC001079, 2003.

823 Perovich, D., Meier, W., Tschudi, M., Farrell, S., Hendricks, S., Gerland, S., Kaleschke, L., Ricker, R.,
824 Tian-Kunze, X., Webster, M., and Wood, K.: Sea ice. Arctic report card 2019, 26–34,
825 <http://www.arctic.noaa.gov/Report-Card>, 2019.

826 Perovich, D. K., and Polashenski, C.: Albedo evolution of seasonal Arctic sea ice, *Geophys. Res. Lett.*,
827 39, L08501, doi:10.1029/2012GL051432, 2012.

828 Proshutinsky, A., Krishfield, R., Timmermans, M. L., Toole, J., Carmack, E., McLaughlin, F., Williams,
829 W. J., Zimmermann, S., Itoh, M., and Shimada, K.: Beaufort Gyre freshwater reservoir: State and
830 variability from observations. *J. Geophys. Res.*, 114, C00A10, doi:10.1029/2008JC005104, 2009.

831 Rampal, P., Weiss, J., Marsan, D., Lindsay, R., and Stern, H.: Scaling properties of sea ice deformation
832 from buoy dispersion analysis. *J. Geophys. Res.*, 113, C03002, doi:10.1029/2007JC004143, 2008.

833 Rampal, P., Dansereau, V., Olason, E., Bouillon, S., Williams, T., Korosov, A., and Samaké, A.: On the
834 multi-fractal scaling properties of sea ice deformation Article, *Cryosphere*, 13(9), 2457–2474, 2019.

835 Salganik, E., Høyland, K. V., and Maus, S.: Consolidation of fresh ice ridges for different scales. *Cold
836 Reg. Sci. Technol.*, 171, 102959, <https://doi.org/10.1016/j.coldregions.2019.102959>, 2020.

837 Screen, J. A., Simmonds, I.: Increasing fall-winter energy loss from the Arctic Ocean and its role in
838 Arctic temperature amplification, *Geophys. Res. Lett.*, 37, L16707, doi:10.1029/2010GL044136,
839 2010.

840 Serreze, M. C., and Meier, W. N.: The Arctic's sea ice cover: trends, variability, predictability, and
841 comparisons to the Antarctic. *Ann. N. Y. Acad. Sci.*, doi:10.1111/nyas.13856, 2018.

842 Spreen, G., Kwok, R., and Menemenlis, D.: Trends in Arctic sea ice drift and role of wind forcing: 1992–
843 2009, *Geophys. Res. Lett.*, 38: L19501, doi: 10.1029/2011GL048970, 2011.

844 Spreen, G., Kaleschke, L., and Heygster, G.: Sea ice remote sensing using AMSR-E 89 GHz channels *J.*
845 *Geophys. Res.*, vol. 113, C02S03, doi:10.1029/2005JC003384, 2008.

846 Spreen, G., Kwok, R., Menemenlis, D., and Nguyen, A. T.: Sea-ice deformation in a coupled ocean–
847 sea-ice model and in satellite remote sensing data, *The Cryosphere*, 11, 1553–1573,
848 <https://doi.org/10.5194/tc-11-1553-2017>, 2017.

849 Steele, M., and Dickinson, S.: The phenology of Arctic Ocean surface warming, *J. Geophys. Res. Oceans*,
850 121, 6847–6861, doi:10.1002/2016JC012089, 2016.

851 Stern, H. L., and Lindsay, R. W.: Spatial scaling of Arctic sea ice deformation, *J. Geophys. Res.*, 114,
852 C10017, doi:10.1029/2009JC005380, 2009.

853 Stern H. L., and Moritz, R. E.: Sea ice kinematics and surface properties from RADARSAT synthetic
854 aperture radar during the SHEBA drift, *J. Geophys. Res.*, 107(C10), 8028,
855 doi:10.1029/2000JC000472, 2002.

856 Strong, C., and Rigor, I. G.: Arctic marginal ice zone trending wider in summer and narrower in winter,
857 *Geophys. Res. Lett.*, 40, 4864–4868, doi:10.1002/grl.50928, 2013.

858 Tschudi, M., Meier, W. N., Stewart, J. S., Fowler, C., and Maslanik, J.: Polar Pathfinder Daily 25 km
859 EASE-Grid Sea Ice Motion Vectors, Version 4, Boulder, CA, USA, NASA National Snow and Ice
860 Data Center Distributed Active Archive Center, <https://doi.org/10.5067/INAWUWO7QH7B>, 2019

861 Tschudi, M. A., Meier, W. N., and Stewart, J. S.: An enhancement to sea ice motion and age products at
862 the National Snow and Ice Data Center (NSIDC), *the Cryosphere*, 14(5), 1519-1536, 2020.

863 Vihma, T., Tisler, P., Uotila, P.: Atmospheric forcing on the drift of Arctic sea ice in 1989–2009,
864 *Geophys. Res. Lett.* 39: L02501, doi: <http://dx.doi.org/10.1029/2011GL050118>, 2012.

865 Wang, J., Zhang, J., Watanabe, E., Mizobata, K., Ikeda, M., Walsh, J. E., Bai, X., Wu, B.: Is the Dipole
866 Anomaly a major driver to record lows in the Arctic sea ice extent? *Geophys. Res. Lett.* 36: L05706.
867 doi:10.1029/2008GL036706, 2009.

868 Woodgate, R. A., Weingartner, T. J., and Lindsay, R.: Observed increases in Bering Strait oceanic fluxes
869 from the Pacific to the Arctic from 2001 to 2011 and their impacts on the Arctic Ocean water column.
870 *Geophys. Res. Lett.*, 39, L24603, doi:10.1029/2012GL054092, 2012.

871 Zhang, Y., Maslowski, W., and Semtner, A. J.: Impact of mesoscale ocean currents on sea ice in
872 high-resolution Arctic ice and ocean simulations, *J. Geophys. Res.*, 104(C8),18409–18429,
873 doi:10.1029/1999JC900158, 1999.

874 Zhao, M., Timmermans, M.-L., Cole, S., Krishfield, R., and Toole, J.: Evolution of the eddy field in the
875 Arctic Ocean’s Canada Basin, 2005–2015, *Geophys. Res. Lett.*, 43, 8106–8114,
876 doi:10.1002/2016GL069671, 2016.

877

878

879

880

881

882

883

884

885

886

887

888

889

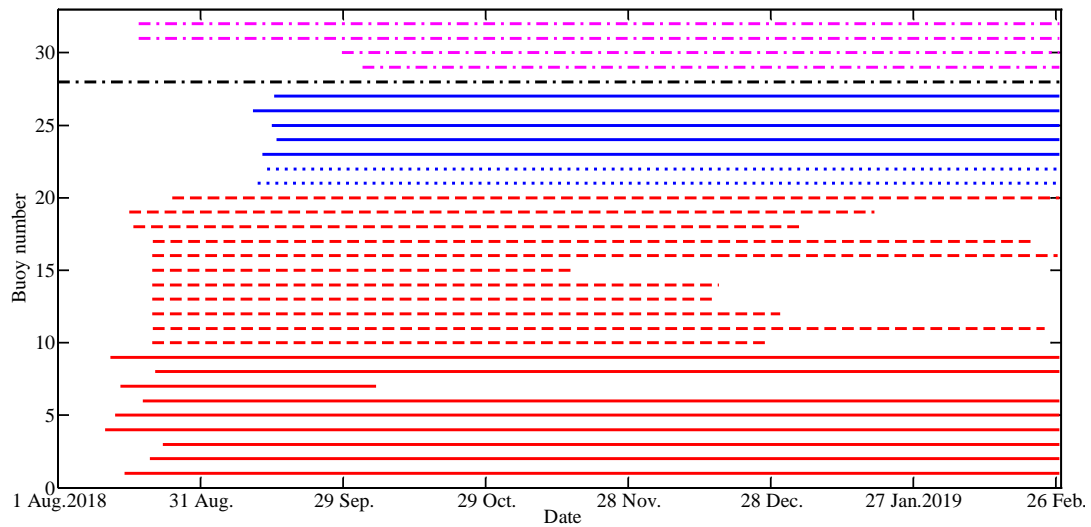
890

891

892

893

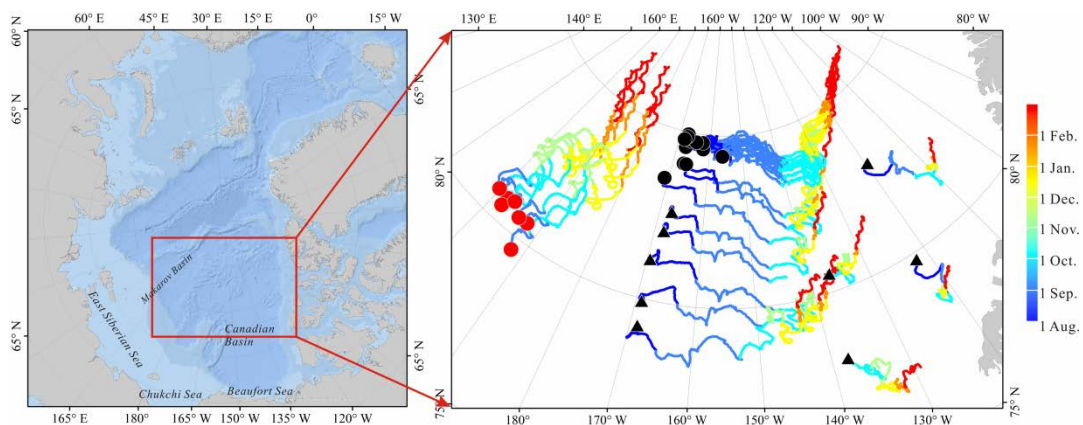
894



895

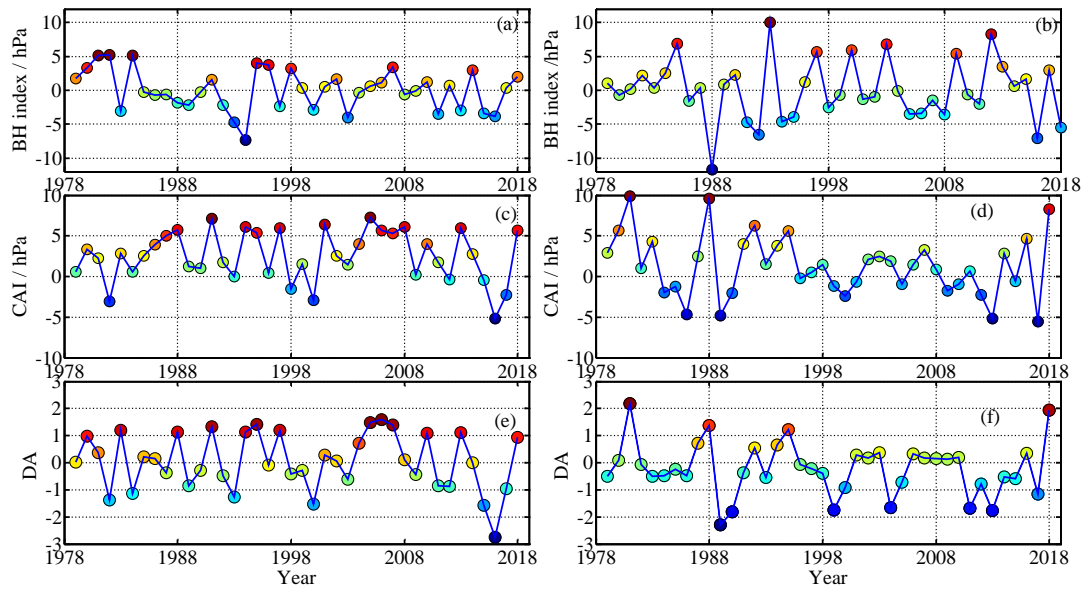
896 **Figure 1 Operational periods of all buoys included in this study. Red lines denote buoys deployed during**
 897 **CHINARE in August 2018; blue lines denote buoys deployed during T-ICE; black line indicates the buoy**
 898 **deployed during CHINARE 2016; purple lines represent IABP buoys. Solid, dashed, short-dashed, and**
 899 **dot-dashed lines denote SIMBA, TUT, SB, and iSVP or other buoys, respectively.**

900



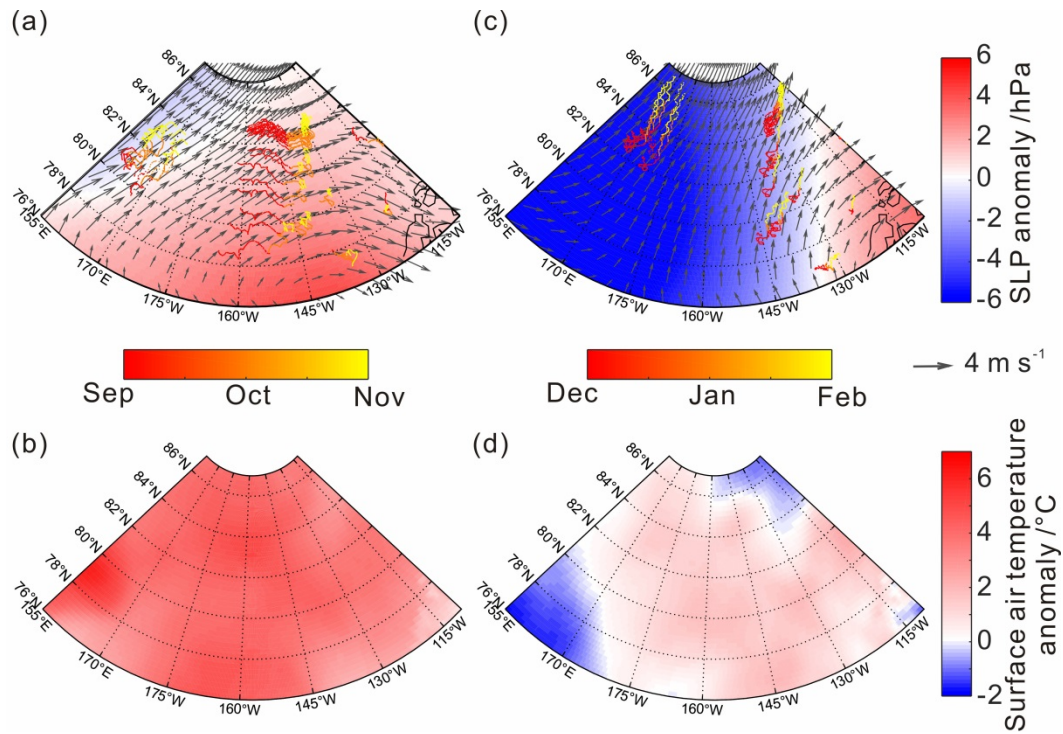
901

902 **Figure 2 Buoy trajectories between deployment sites (indicated by circles and triangles) and buoy locations**
 903 **on 28 February 2019. Trajectories from 15 buoys deployed during CHINARE at locations indicated by black**
 904 **circles and 7 buoys deployed during T-ICE at locations indicated by red circles were used to estimate ice**
 905 **deformation rate. For buoys deployed prior to August 2018, the starting point of the trajectory was set to 1**
 906 **August 2018.**



907

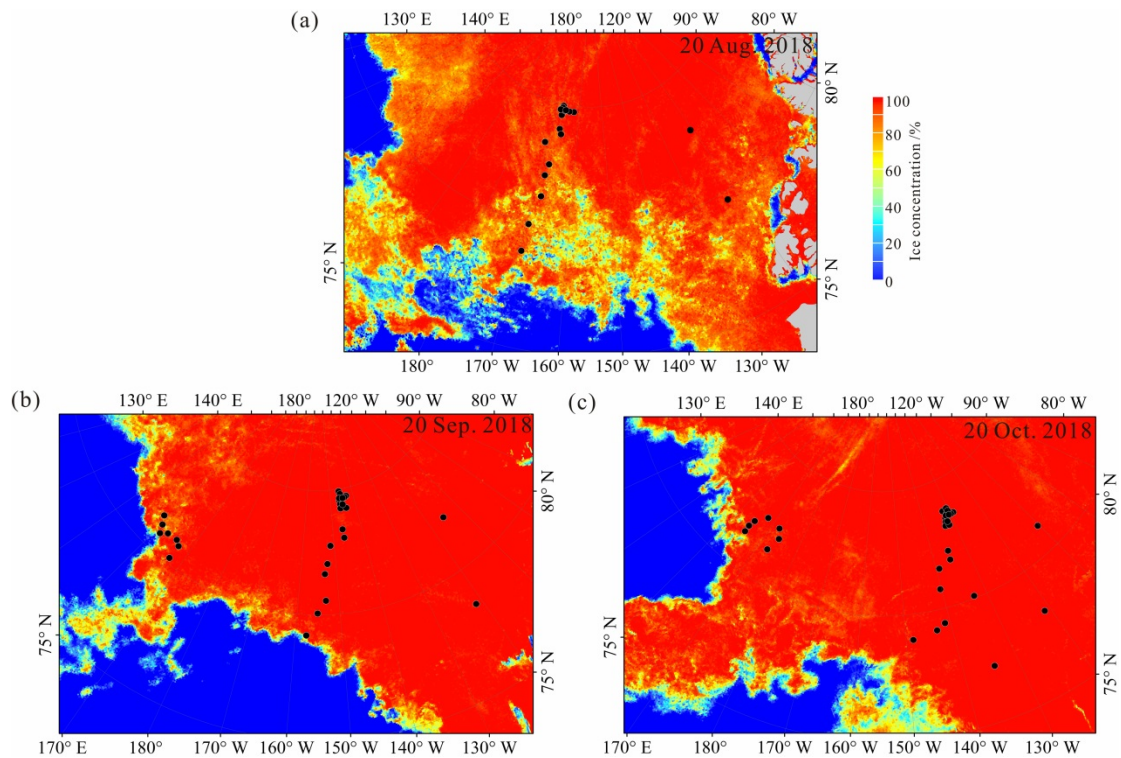
908 **Figure 3** Changes in (a) autumn (SON) and (b) winter (DJF) BH index, (c) autumn and (d) winter CAI, and (e)
 909 **autumn and (f) winter DA from 1979 to 2018.**



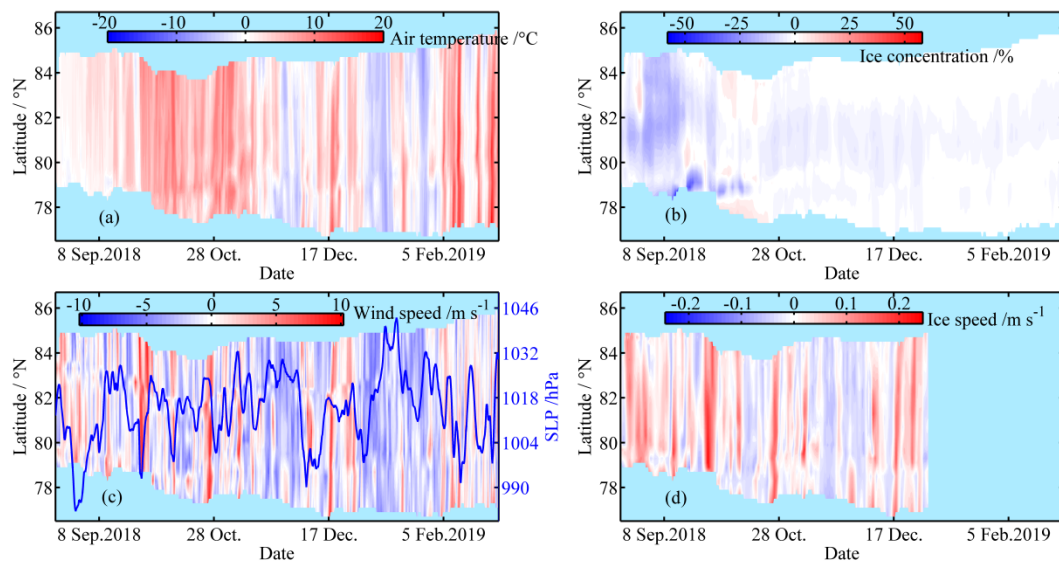
910

911 **Figure 4** Anomalies of (a and c) SLP and (b and d) near-surface air temperature (2 m) over the PAO during
 912 (a and b) autumn 2018 and (c and d) winter 2018/19 relative to 1979–2018 climatology; (a and c) arrows
 913 indicate seasonal average wind vectors and colored lines indicate buoy trajectories through time.

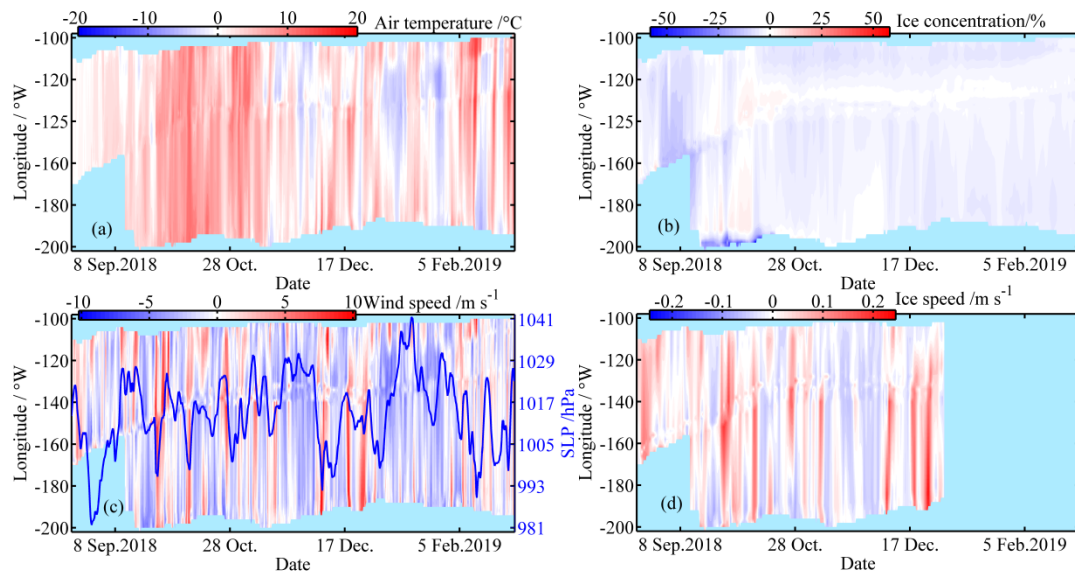
914



915
 916 **Figure 5** Sea ice concentration across the PAO on 20 of (a) August, (b) September, and (c) October, 2018, with
 917 black dots denoting buoy positions on the given days.



918
 919 **Figure 6** Meridional and temporal changes in anomalies of (a) T_{2m} , (b) ice concentration, (c) wind speed, (d)
 920 ice speed in the ice season 2018/19 relative to 1979–2018 climatology; (c) blue line indicates SLP averaged
 921 over the study region.

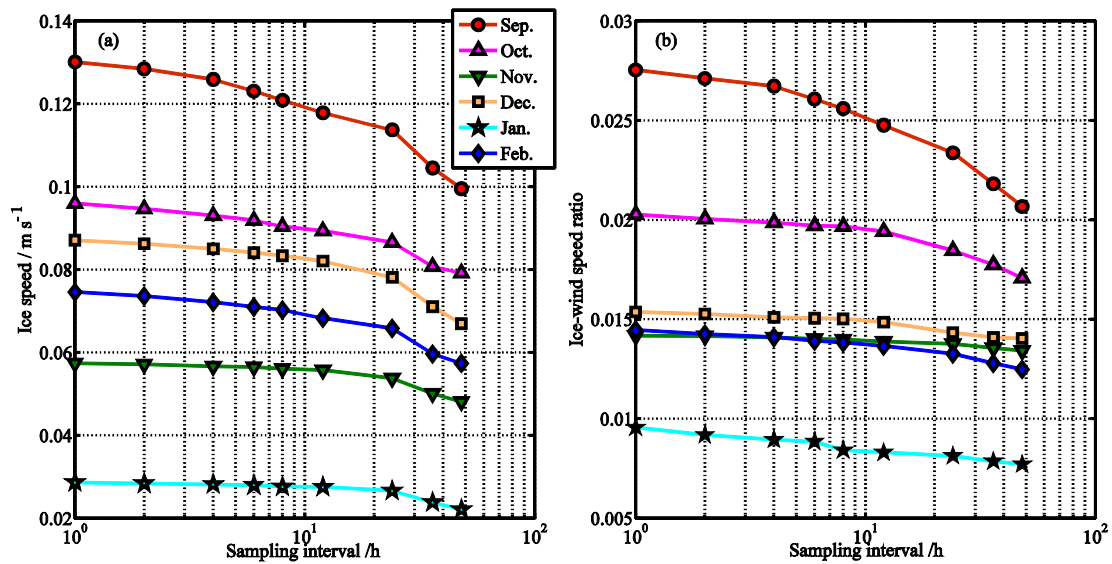


922

923

Figure 7 Same as Fig 2, but for zonal changes. Longitudes with values below -180 denote the eastern Arctic.

924



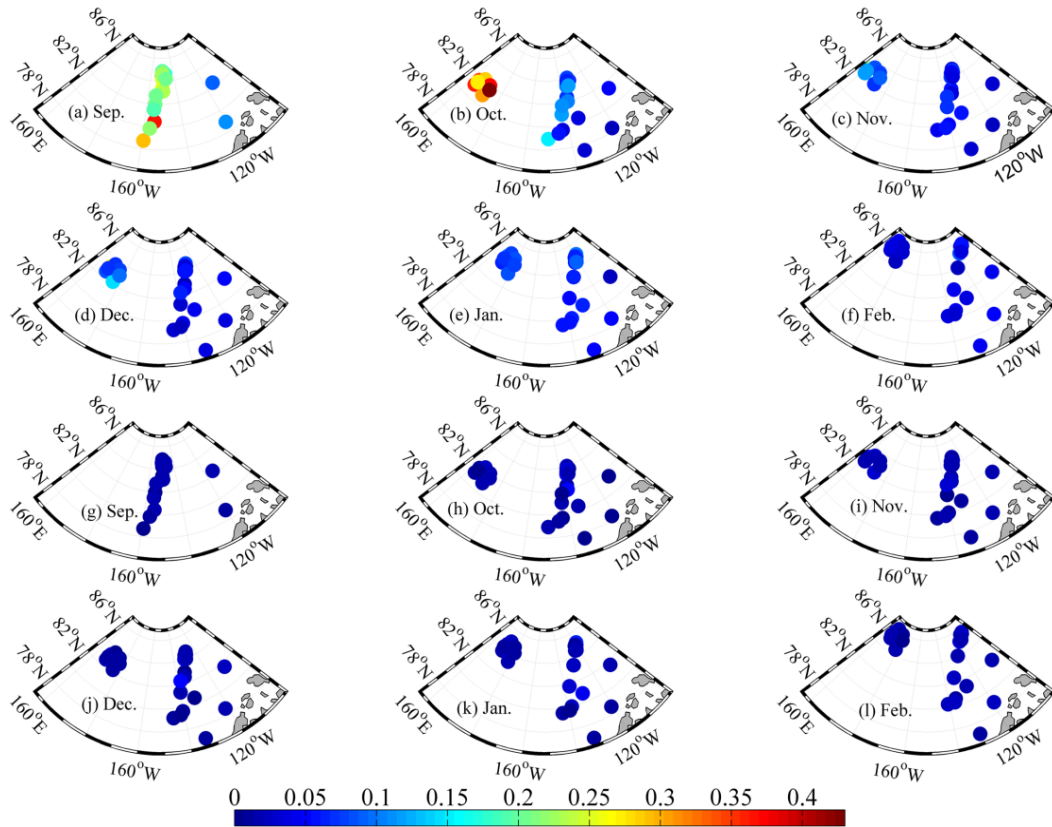
925

926

Figure 8 Changes in (a) ice speed and (b) IWSR as a function of position data resampling interval for various months in 2018/19.

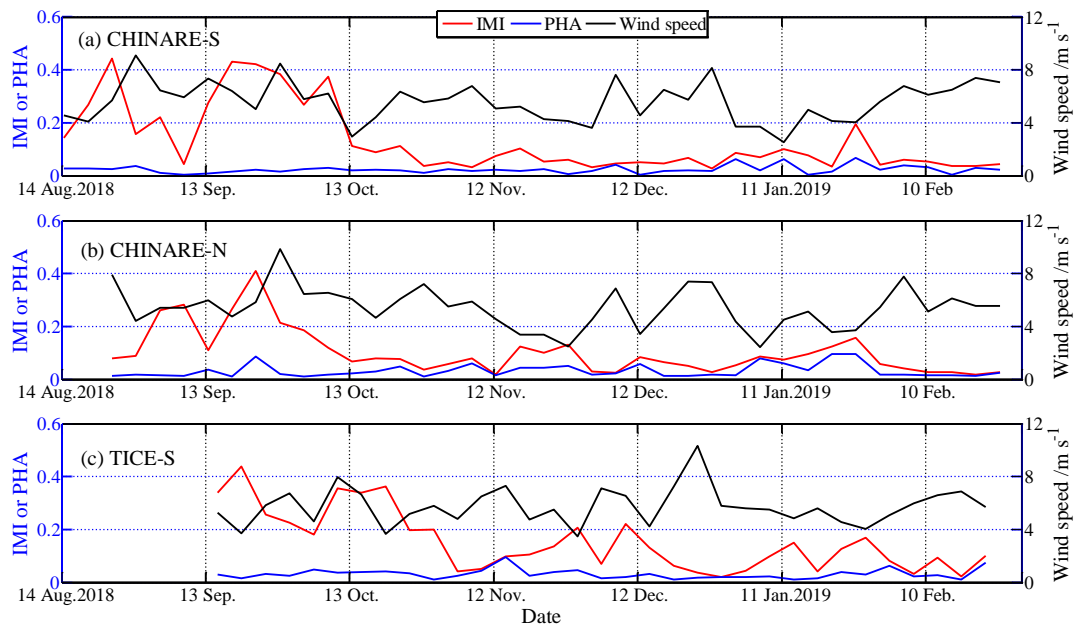
927

928



929

930 **Figure 9** Amplitudes after Fourier transformation of monthly time series of normalized ice velocity at the
 931 **negative-phase inertial frequency (a–f) and positive-phase semidiurnal frequency (g–l) from September 2018**
 932 **to February 2019.**

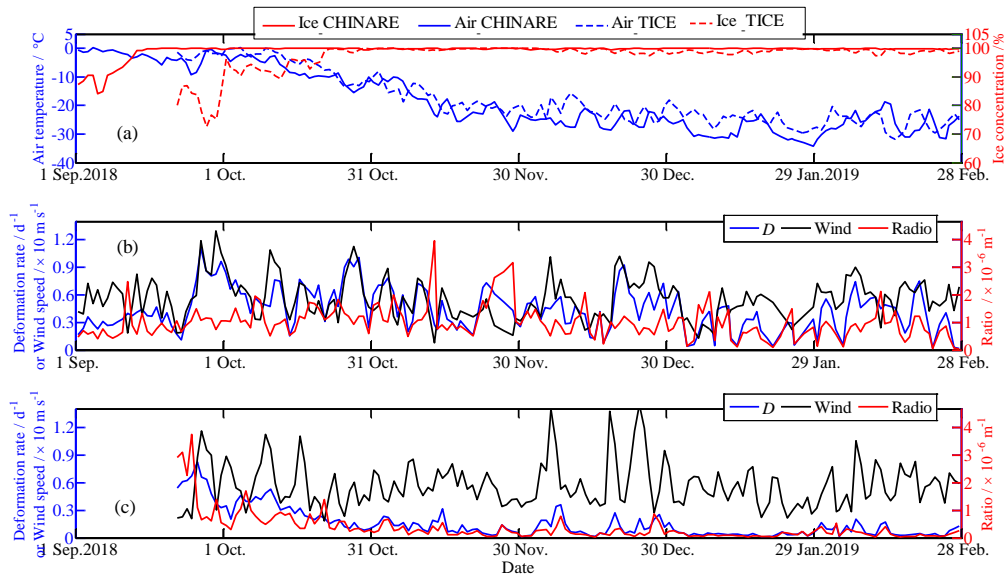


933

934 **Figure 10** Amplitudes after Fourier transformation of normalized ice velocity at the **negative-phase inertial**
 935 **frequency (IMI) and positive-phase semidiurnal frequency (PHA) obtained from the 5-day temporal**
 936 **window, as well as the corresponding wind speed.**

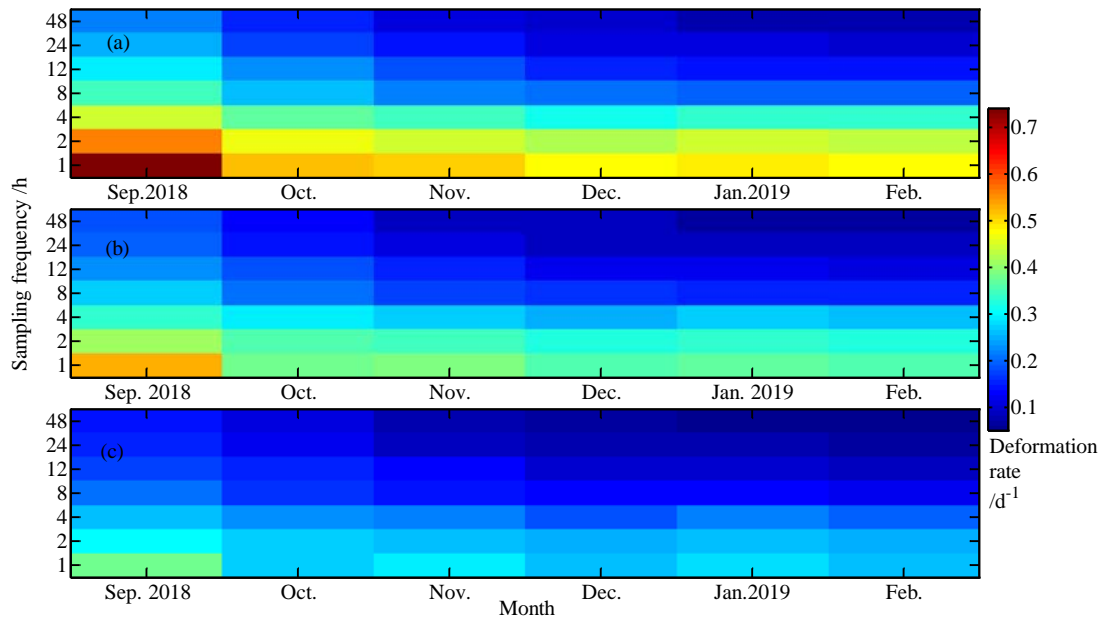
937

938



939

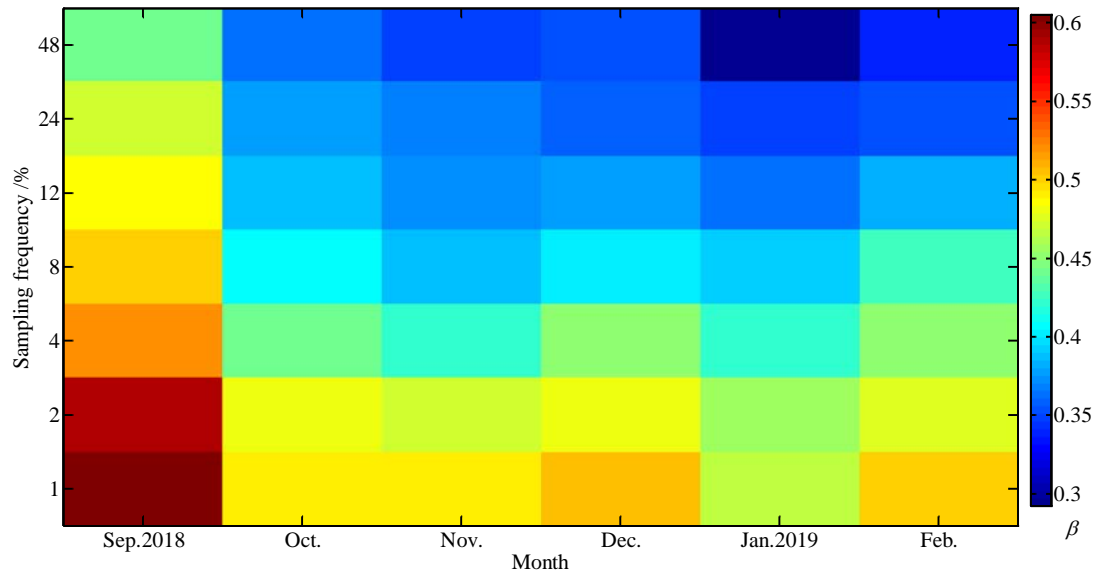
940 **Figure 10-11** (a) Time series of daily average near-surface (2 m) air temperature and ice concentration within
 941 the CHINARE and T-ICE buoy clusters. Ice deformation rate (D), wind speed and their ratio at the 10–20 km
 942 scale for the (b) CHINARE and (c) T-ICE buoy clusters.



943

944 **Figure 11-12** Monthly average sea ice deformation rate calculated from the CHINARE buoy cluster at length
 945 scales of (a) 7.5 km, (b) 15 km, and (c) 30 km using position data resampled at various intervals between 1 and
 946 48 h.

947

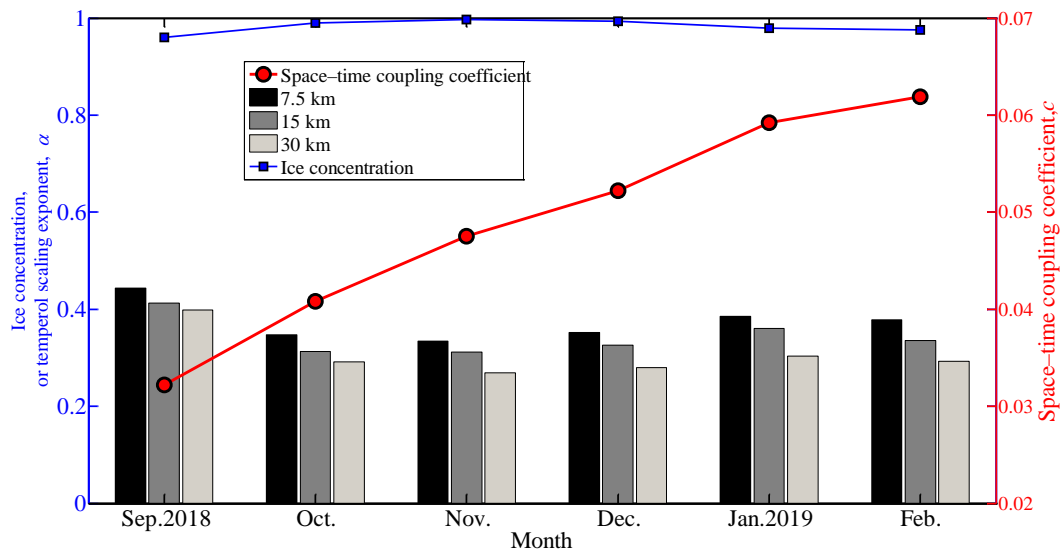


948

949 **Figure 12-13** Changes in monthly spatial scaling exponent as a function of position data resampling frequency

950 obtained from the CHINARE buoy cluster.

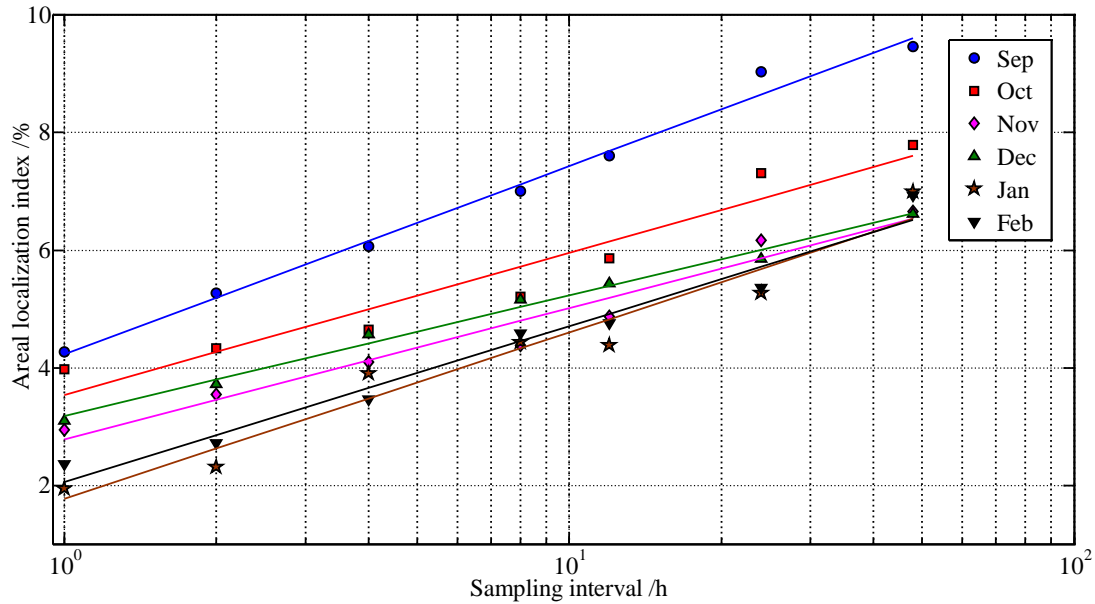
951



952

953 **Figure 13-14** Changes in monthly temporal scaling exponent at various length scales, space-time coupling

954 coefficient, and average ice concentration within the CHINARE buoy cluster.

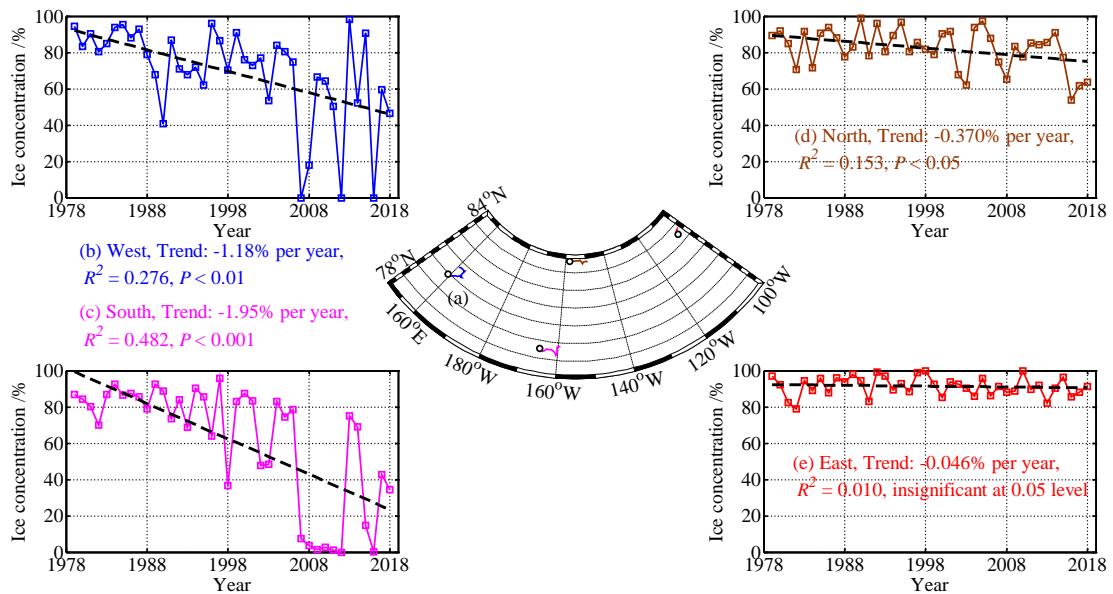


955

956 **Figure 14-15** Changes in monthly (September 2018 to February 2019) areal localization index of ice

957 deformation at a scale of 10–20 km as a function of the position data resampling frequency.

958



959

960 **Figure 15-16** (a) Drift trajectories of the westernmost, southernmost, near northernmost, and easternmost

961 buoys from 1 to 15 September 2018; the northernmost buoy has been omitted because it drifted to the north

962 of 84.5° N, where SMMR ice concentration data prior to 1987 are unavailable; trajectory of the westernmost

963 buoy was reconstructed using the NSIDC ice motion product because this buoy was deployed on 15

964 September 2018; (b–e) Long-term changes in ice concentration along buoy trajectories averaged over 1–15

965 September, with black lines denoting linear trends.

966

967 Table 1. Statistical relationships between IWSR and selected parameters. Significance levels are $P <$
 968 0.001 (***), $P < 0.01$ (**), and $P < 0.05$ (*), and n.s. denotes insignificant at the 0.05 confidence level.
 969 Numbers in parentheses indicate number of buoys used for the statistics.

Month	vs. Lat.	vs. Lon.	vs. W_{10m}	vs. T_{2m}
20 Aug.-30 Sep.	-0.647**(24)	-0.738***(29)	-0.542**(32)	n.s.
Oct.	-0.811***(24)	-0.885***(29)	-0.866***(32)	0.657***(32)
Nov.	-0.777***(23)	-0.765***(28)	n.s.	0.736***(32)
Dec.	-0.736***(22)	-0.829***(27)	n.s.	0.675***(32)
Jan.	n.s.	-0.711**(23)	n.s.	n.s.
Feb.	n.s.	-0.610**(23)	n.s.	n.s.

970